Journal of Alloys and Compounds 1053 (2026) 186163

Contents lists available at ScienceDirect

Journal of Alloys and Compounds

journal homepage: www.elsevier.com/locate/jalcom

First-principles investigation of the structural, dynamic, mechanical, and optoelectronic features of novel K_3SeBr anti-perovskite for photovoltaic and photocatalytic water splitting (solar-to-hydrogen production)

Md. Earshad Ali [a,*], Karim Kriaa [b], Md. Nobiul Islam [a], Md. Shizer Rahman [a], Noureddine Elboughdiri [c], Md. Azizur Rahman [d], Mohamed Benghanem [e,*]

[a] Department of Electrical and Electronic Engineering, Jamalpur Science & Technology University, Jamalpur 2012, Bangladesh
[b] College of Engineering, Imam Mohammad Ibn Saud Islamic University (IMSIU), Riyadh 11432, Saudi Arabia
[c] Chemical Engineering Department, College of Engineering, University of Ha'il, P.O. Box 2440, Ha'il 81441, Saudi Arabia
[d] Department of Electrical and electronic Engineering, Begum Rokeya University Rangpur, Rangpur 5404, Bangladesh
[e] Department of Physics, Faculty of Science, Islamic University of Madinah, Madinah 42351, Saudi Arabia

ARTICLE INFO

Keywords:
Novel K_3SeBr anti-perovskite
Wide bandgap semiconductor
Optoelectronic features
Sunlight-to-hydrogen energy production
Photovoltaic
Sustainable energy element

ABSTRACT

Anti-perovskite compounds have recently gained attention as lead-free, environmentally friendly, and cost-effective candidates for photovoltaic, optoelectronic, and photocatalysis applications due to their structural stability, tunable electronic characteristics, and high optical performance. In this study, the structural, mechanical, electronic, dynamic, optical, and photocatalytic features of the novel K_3SeBr anti-perovskite were systematically investigated utilizing density functional theory (DFT) with GGA-PBE functional. Structural optimization and phonon frequency analysis confirm that K_3SeBr is dynamically stable, while elastic constants indicate robust mechanical stability with ductile behavior (B/G ≈ 1.923). The compound exhibits a 1.726 eV (PBE) and 2.576 eV (HSE06) direct bandgap (Γ-Γ point), suitable for visible-light absorption and solar-driven photocatalytic water splitting. Optical analysis reveals powerful absorption α ≈ (5–0.5)× 10^5 cm^{-1} in the ultraviolet-to-visible light wavelength range, low reflectance (R ≈ 0.04–0.45), and favorable dielectric properties, supporting efficient light harvesting and electron-hole generation. The band edge alignment of the valence and conduction bands in water redox potentials suggests that it is highly efficient for producing hydrogen and oxygen at visible light wavelengths. Furthermore, a novel Al/FTO/SnS_2/K_3SeBr/CuO/Se solar cell was modeled and simulated utilizing SCAPS-1D, achieving an open-circuit voltage (V_o) of 1.1648 V, power conversion efficiency (PCE) of 28.02 %, fill factor (FF) of 82 %, short-circuit current density (J_{sc}) of 29.369 mA/cm^2, and theoretically calculated solar-to-hydrogen (STH) efficiency of 28.89 %. According to results, K_3SeBr is a promising candidate for high-performance, eco-friendly, and lead-free solar cells that are photocatalytic water splitting and optoelectronic devices, combining optical, mechanical, and electronic features suitable for next-generation renewable energy technologies.

1. Introduction

One of the major challenges in the 21st century is to ensure a stable and reliable energy supply. Energy demand has risen dramatically due to quick global population growth and industrialization. For instance, human life required about 15 terawatts (TW) of energy in 2008, a figure that could double by 2050 [1]. The main sources of energy supply today are fossil fuels (such as coal, oil, and gas), renewable sources (solar, wind, and water), and nuclear power. However, a quick transition to a sustainable energy technology system is critical to address climate change and ensure energy security [2]. In this context, hydrogen has gained critical importance as a clean and sustainable energy source worldwide. Its versatile utilization, high energy density, zero greenhouse gas emissions, and applicability in transportation, power generation, and industrial processes are the main reasons for its popularity [3–6]. The International Energy Agency (IEA) recently reported that green hydrogen could play a significant role in reducing carbon emissions if challenges related to infrastructure, supply chains, cost-effective

* Corresponding authors.
E-mail addresses: md.earshadali28@gmail.com, s20111228@bsfmstu.ac.bd (Md.E. Ali), mbenghanem@iu.edu.sa (M. Benghanem).

https://doi.org/10.1016/j.jallcom.2026.186163

Available online 13 January 2026

production methods, and safety can be addressed [7,8].

There are several techniques for producing hydrogen, such as production from fossil fuels, steam reforming, methane cracking, gasification, partial oxidation of heavy oils, and electrolysis of water. However, most methods are complex, expensive, and have negative effects on the environment [9,10]. Photocatalysis, thermochemistry, and electrolysis are relatively more acceptable in the field of clean energy. Among renewable energies, hydrogen is seen as a long-term solution to address future global electricity crises [11,12]. Its effective use is helpful in reducing the dependence on coal, oil, and natural gas in the industrial sector and reducing the harmful impact on the environment. High-performance, low-cost, and sustainable photocatalysis technology is crucial to addressing the challenges of climate change caused by fossil fuels [3,9,13–19]. Hydrogen production is possible more efficiently through water splitting using sunlight, which is environmentally friendly, renewable, and inexhaustible [11,12]. The main research challenge is to develop durable and efficient visible light-activated photocatalysts [11,12]. An ideal photocatalyst can absorb visible light, effectively separate charge carriers, and exhibit improved surface properties for rapid reactions [20,21]. In semiconductor-based photocatalysis, choosing the right materials can control the photoreaction and process energy, which facilitates reduction and oxidation reactions. Significant progress has been made in the past in photocatalysts based on oxide semiconductors (e.g. TiO_2, ZnO, WO_3, and $BiVO_4$) and metal-free or metal sulfides (e.g. CdS, ZnS, SnS_2, and WS_2) [4,22,23].

Perovskite elements have recently made significant progress in photovoltaic and photocatalysis technologies [24–26]. The use of these materials has led to a rapid increase in the efficiency of the associated devices [27]. Specifically, the efficiency of perovskite solar cells has increased from 3.8 % to 26.7 % between 2009 and 2024 [27–30]. In 2019, a solar-to-hydrogen conversion efficiency of 17 % was experimentally achieved using the $MAP(I_{0.85}Br_{0.15})_3$/Si structure [10]. Yet the industrialization of these technologies remains complex, as device durability, degradation in light and air, and the toxicity of some materials remain major challenges. To overcome these limitations, anti-perovskite structure materials are gaining special importance in research [26,31,32]. Here, instead of the conventional ABX_3 structure, the X_3BA anti-perovskite is formed in the opposite configuration, where X is the positive ion (A^+), B is the double negative ion (B^{2-}), and A is the single negative ion (X^-) [33–35]. Such materials are naturally occurring, non-toxic, and have bandgaps suitable for solar cells [36–38]. Recent research indicates that anti-perovskites have great potential for use in many areas of modern technology, including optoelectronics, UV protection, radiation detection, sensors, data storage, superconductivity, fiber optics, solar energy conversion, light detection, hydrogen storage, and photocatalysis [25,26,31,32,39–43].

Considering the several limitations of perovskite elements, the main goal of this research was to find alternative materials that are non-toxic, environmentally friendly, and suitable for photocatalysis, through which the solar-to-hydrogen (STH) conversion efficiency of the material can be evaluated. With this objective in mind, a lead-free and less harmful to the environment K_3SeBr anti-perovskite compound using relatively safe elements such as potassium (K), selenium (Se), and bromine (Br) was proposed in the study. Such anti-perovskites usually form cubic crystal structures and are arranged in the $Pm\bar{3}m$ space group, as shown in Fig. 1(a) [28]. Recently, the Na_3SI-based anti-perovskite Al/Na_3SI/Se structure has been significantly reviewed in water-splitting processes [27]. On the other hand, the hydrogen storage capacities of K_3SH, K_3TeH, and K_3SeH hydrides are 3.24, 2.008, and 2.49 wt%, respectively, which are released at temperatures of 963.88, 672.70, and 793.19 K. Thus, they are considered as potential hydrogen storage materials [42]. In addition, a thin-film ASSB device composed of $LiCoO_2$/Li_3OCl/graphite was prepared using layer-by-layer technology, and it was characterized by an initial discharge capacity of 120 mAh g^{-1} in the voltage range of 2.2–4.2 V [43,44]. More recent findings have shown that anti-perovskite Co_3ZnN provides approximately six times higher hydrogen production rates than Co_4N under visible light, which is evidence of its high photocatalytic activity [45,46]. Furthermore, theoretical analysis has shown that it is possible to significantly enhance the HER efficiency of anti-perovskite Ni_3InN by controlling strain and doping [47].

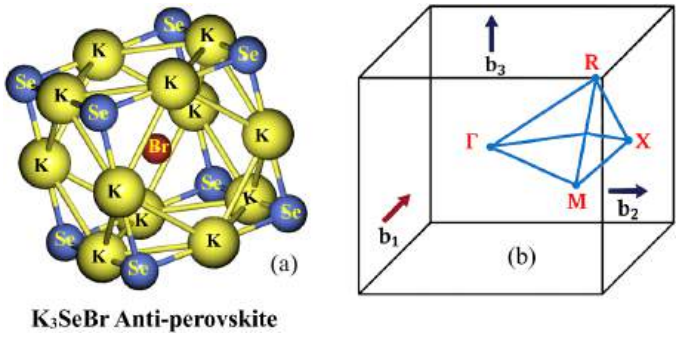

Fig. 1. The K_3SeBr anti-perovskite has (a) the cubic crystal structure and (b) the first Brillouin zone k-path utilized to find out its electronic band structure.

This study evaluated a new, environmentally friendly, and non-toxic anti-perovskite material, K_3SeBr, in a multidimensional manner ((DFT-GGA-PBE) and SCAPS-1D) to gain a full understanding of its energy-conversion capabilities. First, optimization, phonon analysis, and formation energy calculations are performed to ensure the structural, thermal, and dynamic stability of the material. Analysis of its mechanical properties showed that the material is mechanically stable, relatively soft, and has significant load-bearing capacity, which is important for device fabrication and stress-tolerant applications. The direct bandgap 1.726 eV (PBE) and 2.576 eV (HSE06), electron affinity (3.665 eV), and work function obtained from electronic calculations confirm the charge-carrier transfer ability and photo-reaction utility of the material. In optical analysis, high absorption coefficient ($\alpha \approx 5 \times 10^5$ - 0.5×10^5 cm^{-1}), high refractive index ($n \approx 1.5$–1.55), improved dielectric response ($\varepsilon_1(0) = 1.91$, $\varepsilon_1(\infty) = 0.98$), suitable penetration depth ($\delta \approx 2$–5 nm), and low energy loss function ($L_{min} \approx 0.05$, $L_{max} \approx 7.5$) of K_3SeBr ensure its effective light absorption and charge separation in the visible-UV light region. Electron–hole mobility ($\mu_e \approx 38.7$ cm^2/V.s, $\mu_h \approx 8.17$ cm^2/V.s) and effective band gap identify it as a suitable semiconductor for photocatalytic water splitting. In the Al/FTO/SnS_2/K_3SeBr/CuO/Se full device simulation of SCAPS-1D, the device exhibited $J_{sc} = 29.369$ mA/cm^2, $V_o = 1.1648$ V, FF = 82 %, and PCE = 28.02 %. Based on this, the theoretical STH efficiency was found to be ≈ 28.89 %, indicating the efficient photo-energy conversion capability of K_3SeBr. These results show that the combined structural stability of K_3SeBr, coupled with strong optical absorption capabilities, high charge conductivity, and suitable band alignment, makes it dual-use (photovoltaic+photocatalytic) and highly promising as a next-generation energy material. As a result, this research provides important directions for the development of future high-efficiency solar cells, hydrogen production technologies, and safe and sustainable energy devices.

2. Simulation methodology

2.1. The computational technique of K_3SeBr anti-perovskite

In this study, the dynamic, mechanical, electrical, and optical properties of the inorganic anti-perovskite compound K_3SeBr are analyzed in detail based on first-order density functional theory (DFT) [48–50]. This computation was done using Quantum ESPRESSO, which is a powerful and reliable software platform that is widely used in DFT-based numerical calculations. Scalar relativistic ultrasoft pseudo-potential (USPP) (K.pbe-spn-rrkjus_psl.1.0.0.UPF, Se. pbe-dn-rrkjus_psl.1.0.0.UPF, and Br.pbe-dn-rrkjus_psl.1.0.0.UPF) has been used to make mathematical calculations fast and ensure accuracy,

which is very useful to calculate structural optimization, mechanical and phonon stability analysis, and electronic characterization [51]. As well as the functional Perdue-Burke-Ernzerhoff (PBE) of the generalized gradient approximation (GGA) family was chosen for the exchange relation [52], which provides more accurate results than the local density approximation (LDA) [53]. In this study, detailed convergence tests were conducted on all important computational parameters before performing first-principles calculations to ensure the reliability and numerical stability of the obtained results. In the plane-wave-based calculation, the effect on the total energy is examined by changing the cutoff energy (ecutwfc) and the charge density cutoff (ecutrho) step by step. The convergence analysis shown in Fig. 2(a) shows that the total energy converges properly at ecutwfc = 50 Ry and ecutrho = 400 Ry. However, to ensure greater accuracy, this study used higher cutoff values, ecutwfc = 60 Ry and ecutrho = 480 Ry, respectively, for all final calculations [54]. In addition, the convergence of the total energy on a k-point mesh ranging from 1 × 1 × 1–10 × 10 × 10 was tested using a Γ-centered Monkhorst–Pack k-point grid to verify the reliability of the Brillouin-zone sampling. As shown in Fig. 2(b), the energy converges on a 6 × 6 × 6 Γ-centered k-point grid; however, an 8 × 8 × 8 Γ-centered k-point grid is used in all calculations to achieve more stability and reliable results. To ensure high accuracy in electronic self-consistent field (SCF) calculations, a strong convergence criterion is adopted, where 1.0×10^{-8} Ry is used as the SCF convergence threshold [55]. All the above convergence tests have properly verified the computational parameters, which ensures the accuracy and reliability of the results of this study [55]. However, the HSE06 (Heyd–Scuseria–Ernzerhof) hybrid functional is used for accurate bandgap prediction. The norm-conserving pseudopotentials (K.pbe-sp-hgh.UPF, Se.pbe-hgh.UPF, and Br.pbe-hgh.UPF) are applied in these calculations. A 6 × 6 × 6 Γ-centered k-point grid and a 6 × 6 × 6 high q-point mesh are used for Brillouin-zone sampling, which ensures the high accuracy of the HSE06 calculations. Also, it is worth noting that USPP is not effective for optical calculations in the epsilon.x module of Quantum ESPRESSO. The norm-conserving (NC) pseudopotential has been used to ensure high accuracy in the determination of optical properties, as it is able to accurately take into account the properties of especially unoccupied states [56]. Also, a 14 × 14 × 14 k-point grid centered on the Γ-point in the Brillouin zone has been used to analyze optical properties [57–60]. Additionally, the electrostatic potential of the proposed anti-perovskite has also been analyzed. Typically, such an analysis requires a vacuum layer, but in the case of three-dimensional bulk structures, no distinct surfaces or boundaries are created due to the completely periodic extension. Therefore, in this study, the cubic 3D bulk structure of K_3SeBr anti-perovskite has been first transformed into a (1 1 2) supercell and then into a slab along the (0 0 1) direction, where a vacuum layer about 25 Å thick is added along the Z-axis. This slab was only used for electrostatic potential calculations, not structural or other numerical analyses [61–64]. The pseudopotential files used in this study were collected from the official PSlibrary and the Hartwigsen-Goedecker-Hutter PP table of the Quantum ESPRESSO website.

2.2. The computational technique for the STH energy production and photovoltaic efficiency of K_3SeBr component

This research utilized SCAPS-1D software (Version 3.3.11), a well-known semiconductor simulation platform developed by Professor Mark Bergelman. This software was selected to analyze the photovoltaic performance and STH conversion efficiency of the recommended K_3SeBr element. SCAPS-1D was considered a suitable choice due to its comparable results with previous studies and its easy compatibility with other programs [65–67]. First, a K_3SeBr-based solar cell structure was designed in SCAPS-1D, where the semiconductor layers are arranged in the order Al/FTO/SnS_2/K_3SeBr/CuO/Se centered around an anti-perovskite absorber layer. Al (work function 4.1 eV) [68] and Se (work function 5.9 eV) [65] were used as the front and back junction for the purpose of collecting photogenerated charges. The simulation was performed at a temperature of 300 K, AM 1.5 G (1 sun) standard light irradiance, and a frequency of 1.0×10^6 Hz. The proposed K_3SeBr-based solar cell is designed with Al/FTO/SnS_2/K_3SeBr/CuO/Se layering. Two important interface layers, SnS_2/K_3SeBr and K_3SeBr/CuO are added to enhance the performance of this structure. These interfaces reduce recombination, strengthen the internal electric field, and at the same time play a critical role in improving the chemical stability of the device [27,28]. The STH conversion efficiency of the recommended K_3SeBr element was theoretically determined using the short-circuit current density (J_{sc}) of the J-V curve obtained by SCAPS-1D. This software supports modeling of n-type, p-type, or intrinsic semiconductor elements with up to seven layers. The software mathematical model relies on three main differential equations: the transport, Poisson, and continuity equation. These equations give the opportunity to analyze the charge transport, electric field distribution, and overall device performance of solar cells in a simple and clear way [65–69].

3. Result and discussion

3.1. Structural characteristic of K_3SeBr anti-perovskite

In Fig. 1(a) is the cubic structure of anti-perovskite K_3SeBr, which crystallizes in the $Pm\bar{3}m$ space group. In this type of cubic crystal structure, the highest five atoms are arranged in a unit cell. In the structure, the potassium (K) cations are located at (0.5, 0, 0), (0, 0.5, 0), and (0, 0, 0.5) positions and occupy the octahedral voids. On the other hand, the selenium (Se) atom is located at (0, 0, 0) positions and fills the face-centered voids. The bromine (Br) ion is located at (0.5, 0.5, 0.5) point and fills the halogen site at the center of the unit cell. In Fig. 1(b) is the Brillouin zone of a cubic crystal, which plays an important role in the analysis of the band structure. In this study, the Γ-X-M-Γ-R-X path is followed for the band structure. In Fig. 2(a) are the total energy changes with the change in cell parameters. The lower the energy value, the more stable the structure is considered [73–75]. Convergence tests were performed by varying cell parameters and k-point grids to ensure structural accuracy. In Table 1 are the best lattice constant (a), unit cell volume (V_o), and total energy (E_o) obtained in this study, as well as a comparison with the values reported in some previous studies. A 60 Ry kinetic energy cut-off, 480 Ry charge density cut-off, and 8 × 8 × 8 Monkhorst–Pack k-point grid were used for structural optimization.

3.2. Phonon dispersion of K_3SeBr anti-perovskite

Phonon scattering pertains to the collective oscillations of atoms within a crystal lattice and the way these oscillations enable the transfer or dissipation of energy [76,77]. A comprehensive understanding of phonon behavior, encompassing phonon dispersion and lattice dynamics, is essential for assessing a material's thermodynamic stability and vibrational properties. This study involved meticulous adjustment of the atomic locations and lattice properties of the K_3SeBr anti-perovskite compound prior to performing phonon calculations [78–80]. The phonon band structure was delineated along the conventional Γ–X–M–Γ–R–X trajectory in the Brillouin zone (Fig. 2(b)), offering insights into phonon propagation directions and vibrational energy distribution. The examination of the phonon dispersion curves indicates the absence of negative or imaginary frequencies in the spectrum. This unequivocally indicates that the material possesses dynamic stability and is devoid of structural instabilities. This stability verifies that K_3SeBr is both mechanically and thermodynamically robust, making it appropriate for incorporation into high-performance devices. The strong lattice vibrations and lack of anomalous phonon modes indicate high reliability for use in optoelectronic devices, photovoltaic systems, and photocatalytic processes, where stable atomic-scale energy transfer is essential for sustained efficiency and longevity.

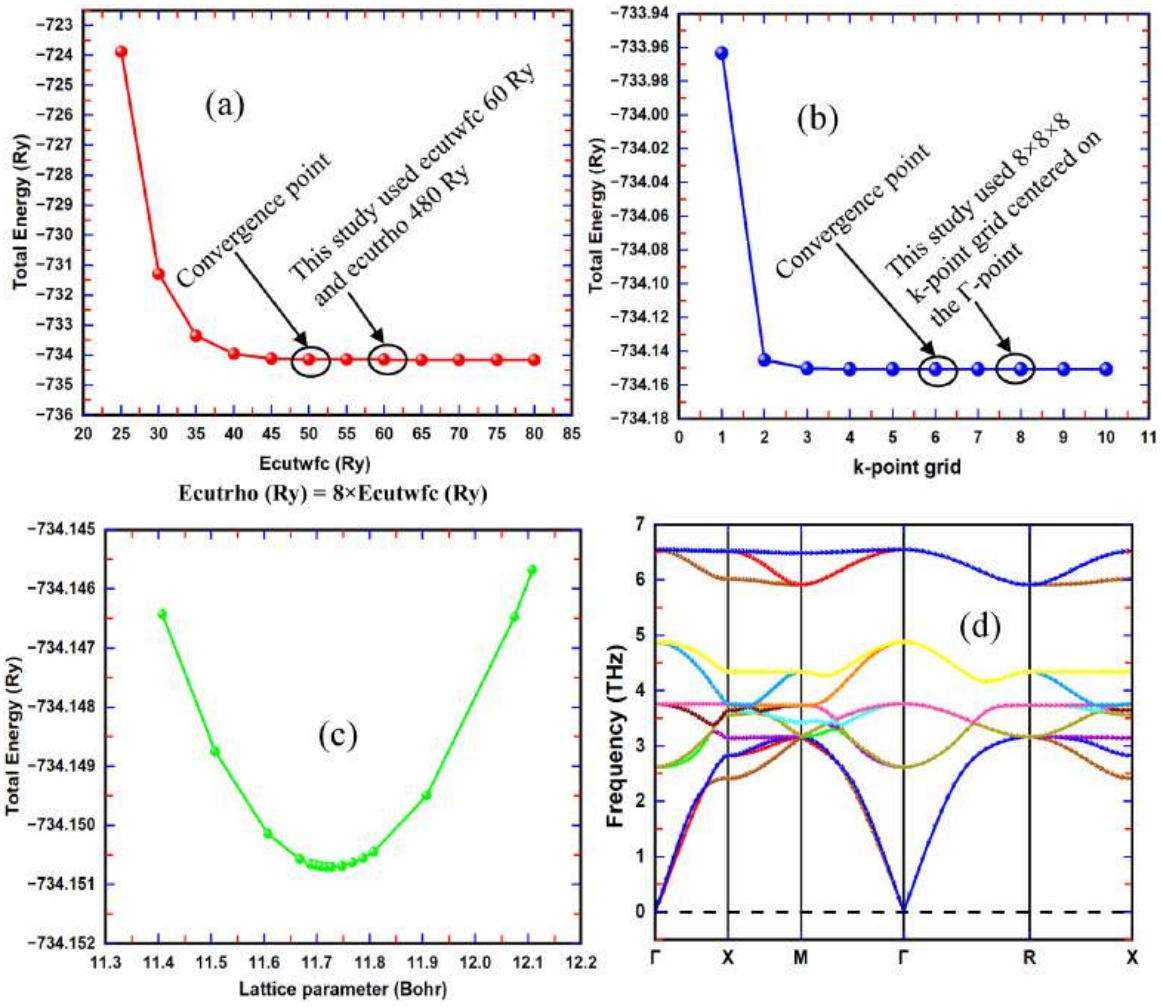

Fig. 2. Characteristics of (a) the ecutwfc and ecutrho, (b) the K-point grid, (c) the cell parameter, and (d) the phonon frequency of the K_3SeBr anti-perovskite.

Table 1
The comparison of unit cell volume, total energy, and lattice constant of K_3SeBr obtained in this and earlier published works.

Compound	a_0 (Å) (a = b = c)	Unit cell-volume V_o (a.u)^3	Total energy E_0 (Ry)	Reference
Na_3SI	5.321	1016.77	-345.73647	[27]
Na_3SBr	5.2576	980.80	-611.34799	[28]
K_3SeBr	6.2048	1612.1492	-734.150703	This work
Na_3OI	4.74	718.697	-5166.15	[70]
Na_3OBr	4.57	-	-	[71]
Na_3OCl	4.53	-	-	[72]
K_3OI	5.37	1045.029	-3614.13	[70]

3.3. Mechanical characteristics of K_3SeBr anti-perovskite

Analyzing the elastic or mechanical properties of a solid compound is extremely important, as these properties play a fundamental role in calculating the crystal structural stability, response to external forces, and its usability in engineering [81,82]. In particular, the determination of elastic constants using Quantum ESPRESSO's thermo_pw module allows for a precise understanding of the molecular-level stiffness, flexibility, and deformation resistance of materials. The information is crucial not only for fundamental physics but also for contemporary technological applications, such as nanoelectronics, aerospace structures, flexible electronics, thermomechanical coatings, and various types of mechanical sensor designs. By analyzing elastic properties, it is possible to determine the ductility, brittleness, nature of chemical bonds, anisotropy, and sound velocity of a material. This information indicates how mechanically strong a material is and how reliable it is for technical use. In this study, the mathematical equations necessary for determining the mechanical properties of K_3SeBr were applied, and the

Table 2
The mechanical characteristics of K_3SeBr anti-perovskite.

Elastic/mechanical properties	Elastic/mechanical properties value
Elastic constant C_{11}	28.745 GPa
Elastic constant C_{12}	1.776 GPa
Elastic constant C_{44}	2.813 GPa
$C_{11} - C_{12}$, $C_{11} + 2\,C_{12}$, and C_{44}	26.968, 32.297, and 2.813 (GPa) which > 0
Bulk modulus, B	10.765 GPa
Shear modulus for Voigt approximation, G_v	7.082 GPa
Shear modulus for Reuss approximation, G_R	4.116 GPa
Shear modulus For Voigt-Reuss-Hill average, G	5.599 GPa
Young's modulus, E	14.188 GPa
Poission's ratio, V	0.267
Pugh's ratio, (B/G)	1.923
Cauchy pressure, $C_{12} - C_{44}$	−1.0373 GPa
Zener anisotrop, A	0.208
Universal aniostropy index, A^U	3.595
Shear sound velocity, V_S	1707.845 ms^{-1}
Longitudinal sound velocity, V_L	3081.740 ms^{-1}
Average Debye sound velocity, V_m	1771.552 ms^{-1}
Debye temperature, Θ_D	145.362 K

results are presented in Table 2 and Fig. 3 [83–92]:

Mechanical stability criteria (Born criteria; cubic crystal):

$$C_{11} - C_{12} > 0,\ C_{11} + 2\,C_{12} > 0,\ \text{and}\ C_{44} > 0 \quad (1)$$

Bulk modulus:

$$B = \frac{C_{11} + 2C_{12}}{3} \quad (2)$$

Shear modulus (G): For Voigt approximation:

$$G_V = \frac{C_{11} - C_{12} + 3C_{44}}{5} \quad (3)$$

For Reuss approximation:

$$G_R = \frac{5(C_{11} - C_{12})C_{44}}{4C_{44} + 3(C_{11} - C_{12})} \quad (4)$$

For Voigt-Reuss-Hill average:

$$G = \frac{G_V + G_R}{2} \quad (5)$$

Young's modulus:

$$E = \frac{9BG}{3B + G} \quad (6)$$

Poission's ratio:

$$V = \frac{3B - 2G}{2(3B + G)} \quad (7)$$

$$\text{Ductility Vs.Brittleness(Pugh's ratio)}: \frac{B}{G} > 1.75;\ \text{ductile and If}\ \frac{B}{G} < 1.75;\ \text{barittle} \quad (8)$$

Cauchy pressure (bound nature):

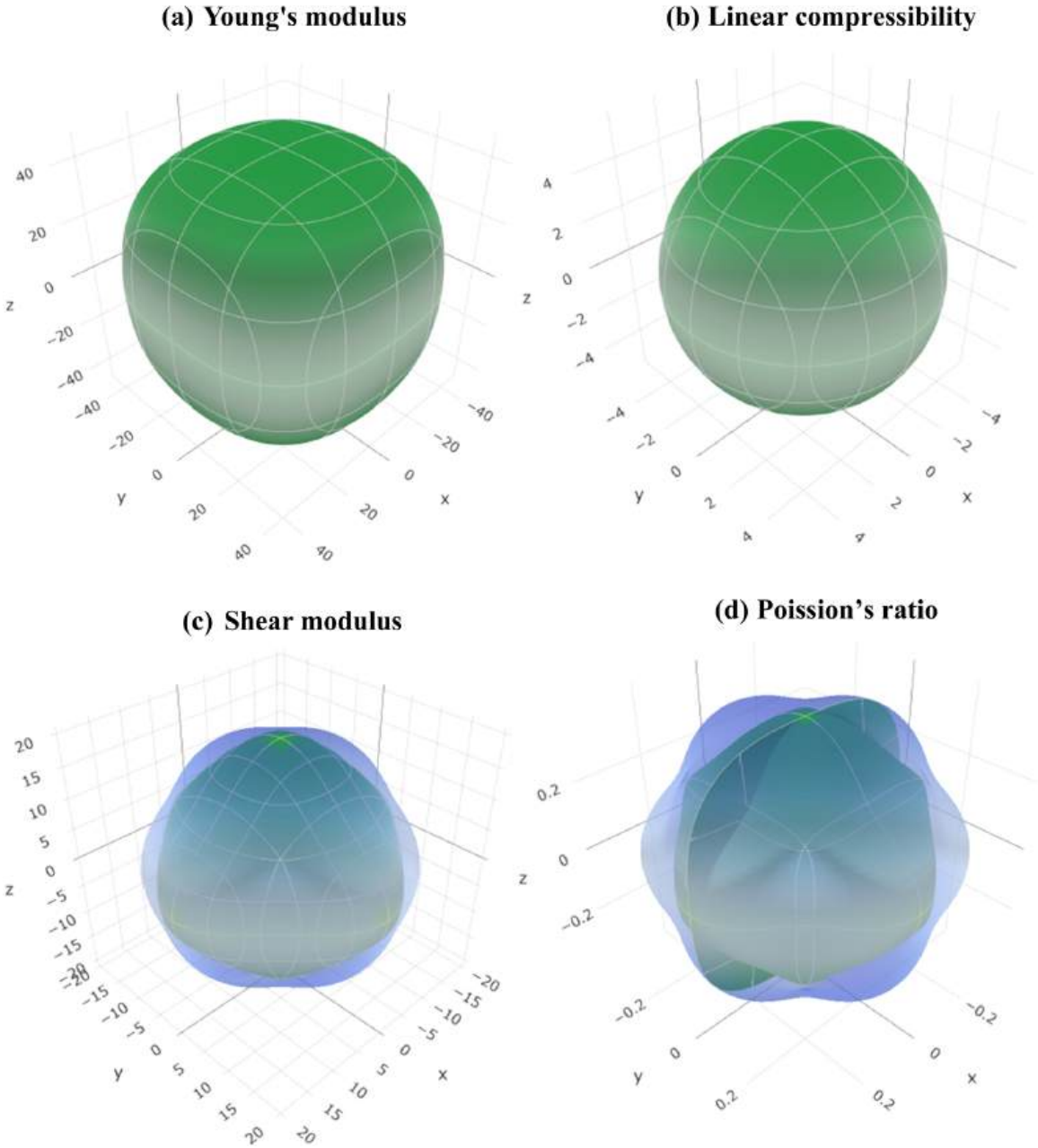

Fig. 3. The K_3SeBr tensors of (a) Young modulus, (b) linear compressibility, (c) Shear modulus, and (d) Poisson ratio.

$C_{12} - C_{44} > 0$; metallic and $C_{12} - C_{44} < 0$; covalent/directional bonding tendency (9)

Elastic anisotropy:

$$\text{Zener anisotrop} : A = \frac{2C_{44}}{C_{11} - C_{12}} \text{and Universal aniostropy index} : A^U = 5\frac{G_V}{G_R} + \frac{B_V}{B_R} - 6 \quad (10)$$

Sound velocity & Debye temperature: Shear sound velocity:

$$V_S = \sqrt{\frac{G}{P}} \quad (11)$$

Longitudinal sound velocity:

$$V_L = \sqrt{\frac{3B + 4G}{3\rho}} \quad (12)$$

Average sound velocity:

$$V_m = \left[\frac{1}{3}\left(\frac{2}{V_s^3} + \frac{1}{V_L^3}\right)\right]^{-\frac{1}{3}} \quad (13)$$

Debye temperature:

$$\Theta_D = \frac{h}{K_B}\left(\frac{3n}{4\pi V}\right)^{\frac{1}{3}} V_m \quad (14)$$

Here, h and K_B are the Planck and Boltzman constants, respectively, n is the atom number per unit cell, V is the unit cell volume, and ρ is the density [83–92].

As seen in Table 2, the compound exhibits exceptional mechanical stability, underscoring its capacity to withstand deformation under applied loads. The moderate bulk modulus and somewhat low shear modulus indicate that the material is mechanically flexible while remaining adequately robust, providing structural flexibility and durability. The ductile characteristics, indicated by the Pugh ratio (B/G ≈ 1.923) and the Poisson ratio (≈0.267), confirm the material ability to withstand stress and strain without fracturing, which is particularly beneficial for the fabrication of practical devices, especially in thin-film solar cells and flexible optoelectronic devices. The computed elastic constants adhere to the Born stability criterion, affirming the inherent mechanical integrity of the structure. The moderate Young modulus (≈14.19 GPa) signifies that the material can experience little deformation without compromising its integrity, which is advantageous for preserving contact interfaces and averting delamination in multilayered devices. The negative Cauchy pressure indicates directional bonding traits that may affect anisotropic mechanical responses, a consideration that can be utilized in material processing to enhance device performance. The calculated sound velocities and Debye temperature (about 145 K) indicate advantageous lattice dynamics and phonon transmission, essential for thermal regulation in optoelectronic and photocatalytic applications. Excellent thermal conductivity and moderate lattice rigidity contribute to the reduction of heat accumulation during device operation, thereby improving efficiency and operational lifespan. These mechanical characteristics collectively show that the material is structurally stable and adaptable for incorporation into photovoltaic cells, photocatalytic layers, and other energy-conversion devices where mechanical reliability is essential. The amalgamation of ductility, stability, and advantageous thermal properties highlights the compound's promise as a resilient and pragmatic option for next-generation energy and optoelectronic materials [83–92].

3.4. Thermodynamics stability and formation energy of K_3SeBr anti-perovskite

The formation energy, represented as (ΔE_f and $\Delta E_f^{per\ atom}$), serves as a critical parameter for evaluating the thermodynamic stability of a material. In this work, the formation energy of the K_3SeBr anti-perovskite was calculated using density functional theory (DFT) by considering the total energy contributions of the constituent elements, as described in Eqs. (15) and (16) [93–96]. According to the results summarized in Table 3, the total formation energy of K_3SeBr is found to be −14.44 eV, while the formation energy per atom is −2.888 eV/atom. The negative sign of these values confirms that the compound is thermodynamically favorable, indicating that K_3SeBr can spontaneously form under standard conditions. The observed negative formation energy also implies the presence of strong chemical interactions between potassium, selenium, and bromine atoms in the crystal lattice, reflecting robust chemical bonding and overall structural stability. These results not only establish the energetic favorability of K_3SeBr formation but also highlight its potential durability and resilience, suggesting that this material is well-suited for practical applications in photovoltaic, photocatalytic, and optoelectronic devices.

Formation Energy,

$$\Delta E_f = E_{tot}^{K_3SeBr} - \left(3E_{tot}^{K} + E_{tot}^{Se} + E_{tot}^{Br}\right) \quad (15)$$

Formation Energy per Atom,

$$\Delta E_f^{per\ atom} = \frac{E_{tot}^{K_3SeBr} - \left(3E_{tot}^{K} + E_{tot}^{Se} + E_{tot}^{Br}\right)}{5} \quad (16)$$

3.5. Electronic characteristics of K_3SeBr anti-perovskite

The electronic behavior of a material is mainly governed by how its electrons are arranged, distributed, and move within different energy levels. These factors define its electrical conductivity and its overall response to external electric and magnetic fields. To examine these characteristics, three key descriptors are generally used: the band structure, the electrostatic potential, and the partial density of states (PDOS) [97–99]. In this work, special attention has been given to the electrostatic potential profile because it provides direct insight into the electron affinity of the material, an essential parameter for evaluating its suitability in photovoltaic and photocatalytic applications [97–99]. A comprehensive study of these electronic characteristics was therefore necessary to determine whether the newly proposed K_3SeBr anti-perovskite compound can perform effectively in modern electronic and optoelectronic devices [97–99].

3.5.1. Band structure of K_3SeBr anti-perovskite

In Fig. 4(a) is the electronic band structure of the novel K_3SeBr anti-perovskite, with the Fermi level referenced at zero energy. The analysis reveals that both the VBM maximum and the CBM minimum are positioned at the Γ point, unequivocally identifying K_3SeBr as a direct band-gap semiconductor. The calculated band gap is 1.726 eV (GGA-PBE) and 2.576 eV (HSE06), placing it well within the optimal range for visible-light absorption [100–104]. The significance of a direct band gap lies in its ability to facilitate vertical electronic transitions without phonon

Table 3
The formation energy and total energy of K_3SeBr anti-perovskite.

Material	Total energy (Ry)	Total energy (eV)	Atom number	Formation energy (eV)	Formation energy per atom (eV)
K_3SeBr	-734.15070	−9986.70	5	−14.44	−2.888
K	-58.700056	−798.36	1	-	-
Se	-258.19834	−3511.51	1	-	-
Br	-298.82173	−4065.67	1	-	-

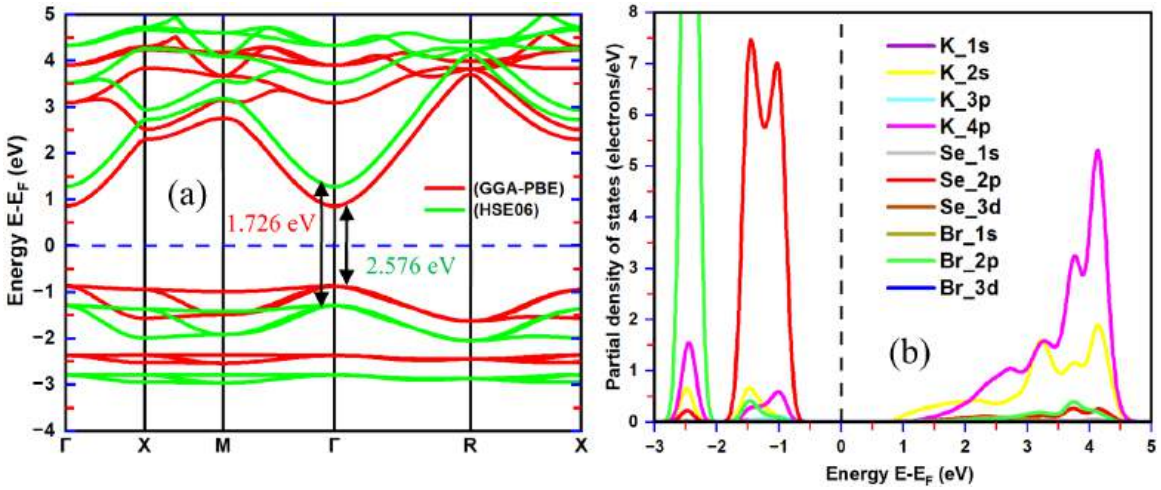

Fig. 4. (a) Electronic band structure and (b) PDOS for K3SeBr anti-perovskite.

assistance, enabling highly efficient excitation of electrons, which is pivotal for optoelectronic devices, photocatalytic processes, and nanoscale semiconductor applications. From a photocatalytic perspective, the band gap of a material critically governs its ability to drive water-splitting reactions. While the thermodynamic minimum energy required for hydrogen evolution is 1.23 eV, practical applications demand a slightly higher band gap to overcome overpotential losses and ensure effective electron–hole separation. The range of 1.6–3.0 eV is widely recognized as ideal because it balances sufficient visible-light absorption with the generation of charge carriers at energies adequate to drive redox reactions efficiently. Materials exceeding ~3.1 eV typically exhibit limited visible-light activity, drastically reducing their photocatalytic effectiveness [42,45,105,106]. In this context, the band gap of K_3SeBr equal to 1.726 eV (PBE) and 2.576 eV (HSE06) not only confirms its suitability as a visible-light-responsive material but also highlights its dual potential in high-performance optoelectronic applications and sustainable photocatalysis. The predicted electronic structure and direct band gap suggest that electrons can be excited quickly, that recombination losses are low, and that energy alignment is good for converting solar energy. Consequently, K_3SeBr emerges as a highly promising candidate for next-generation electronic devices, advanced optoelectronic systems, and efficient solar-driven hydrogen production, underscoring its novelty and practical relevance in contemporary material science [42,45,105,106].

3.5.2. *The features of the partial density of state (PDOS) of the K_3SeBr component*

In Fig. 4(b) are the PDOS for the K_3SeBr anti-perovskite, highlighting the specific contributions of the potassium (K), selenium (Se), and bromine (Br) atomic orbitals. The horizontal axis represents the energy relative to the Fermi energy (E-E_F), with E_F set as the zero reference point [98,99]. Analysis of the PDOS reveals that the valence band is predominantly formed by the K_2s, K_4p, Se_2p, and Br_2p orbitals. The electronic density is especially pronounced in the energy interval between −0.7 and −2 eV, confirming that the orbitals of K, Se, and Br are the primary contributors to the valence band states, while other orbitals have a minimal effect. Conversely, the conduction band extends roughly from 1 to 4.5 eV and is dominated by the same set of orbitals, showing that these orbitals effectively control the electronic properties of K_3SeBr. The absence of states at the Fermi level establishes a well-defined band gap, verifying the semiconducting nature of the material. Given that semiconductors with band gaps around 2.5 eV generally perform well in optoelectronic applications, the PDOS results indicate that K_3SeBr is a promising candidate for such devices, offering favorable electronic characteristics for efficient charge transport and light absorption [107,108].

3.5.3. *The mobility and effective mass of carriers in K_3SeBr anti-perovskite*

The effective masses of electrons (m_e) and holes (m_h) have been determined by applying parabolic fitting to the band-edge region from the band structure of K_3SeBr anti-perovskite (Fig. 4(a)). Then, the effective density of states (N_{CB}) of the conduction band and the effective density of states (N_{VB}) of the valence band were calculated at a temperature of 300 K. The carrier scattering time (τ) at 300 K in typical semiconductor materials is found to be between 10^{-13} and 10^{-14} s. In this study, the mobility of holes (μ_h) and electrons (μ_e) was calculated assuming $\tau = 10^{-14}$ s, which was implemented based on previous experimental and simulation data [104,109–117]. The relevant formulas for the necessary calculations are given below.

Hole/electron effective mass:

$$m^* = h^2 \left[\frac{\partial^2 E(k)}{\partial k^2}\right]^{-1} \tag{17}$$

Conduction Band of states:

$$N_{CB} = 2\left[\frac{2\pi m_e^* K_B T}{h^2}\right]^{\frac{3}{2}} \tag{18}$$

Valence Band of states:

$$N_{VB} = 2\left[\frac{2\pi m_h^* K_B T}{h^2}\right]^{\frac{3}{2}} \tag{19}$$

Mobility of hole/electron:

$$\mu = \frac{e\tau}{m^*} \tag{20}$$

Here K_B is the Boltzmann constant and e is the electron charge [104,109–117]. The values of m_e, N_{CB}, N_{VB}, and m_h obtained from the band structure data, as shown in Fig. 4(a), are presented in Table 4. These values were selected to calculate the theoretical STH power conversion efficiency through modeling and performance evaluation of K_3SeBr--based solar cells.

As presented in Table 4, the K_3SeBr anti-perovskite exhibits a notable asymmetry in the effective masses of electrons and holes. The relatively small effective mass of electrons promotes high mobility, resulting in an electron mobility of approximately $\mu_e = 38.7\ cm^2/V.s$, whereas the larger effective mass of holes restricts their movement, giving a hole mobility of $\mu_h = 8.17\ cm^2/V.s$. This pronounced difference in carrier dynamics enables efficient electron transport, which is critical for swift charge collection in devices such as solar cells and photodetectors.

Table 4
The DOS, mobility, and effective mass of K_3SeBr anti-perovskite.

Structure	Hole effective mass, m_h^*	Electron effective mass, m_e^*	VB effective DOS, N_{VB} (1/cm^3)	CB effective DOS, N_{CB} (1/cm^3)	Hole mobility, μ_h (cm^2/Vs)	Electron mobility, μ_e (cm^2/Vs)
K_3SeBr	2.15 m_0	0.455 m_0	2.5×10^{19}	7.68×10^{18}	8.17	38.7

Furthermore, the calculated effective density of states in both the valence and conduction bands supports these transport characteristics. A higher density in the valence band enhances hole-mediated optical transitions, complementing the rapid electron conduction. Together, these features establish K_3SeBr as a material with excellent charge separation capabilities and high-speed carrier transport, making it highly suitable for applications in photovoltaics, photocatalysis, and various optoelectronic devices [118–121].

3.5.4. *Electrostatic potential of K_3SeBr anti-perovskite*

The work function, vacuum energy, Fermi level, ionization energy, and electron affinity of the K_3SeBr component were extracted from the slab model shown in Fig. 5(a). The evaluated values are summarized in Fig. 5(b) and Table 5. These energy parameters are particularly important for examining whether the VBM and CBM align with the redox potentials required for oxygen and hydrogen evolution in photocatalytic water splitting. To verify this compatibility, the standard mathematical expressions used to calculate these energy levels are employed, as outlined in [122,123].

$$\text{Work Function: } \phi = E_{vacumm} - E_{Fermi} \quad (21)$$

$$\text{Electron affinity: } EA = E_{vacumm} - E_{CBM} \quad (22)$$

$$\text{Ionization energy: } IE = E_{vacumm} - E_{VBM} \quad (23)$$

Here, E_{VBM} and E_{CBM} denote the valence band maximum and conduction band minimum, respectively [122,123]. As seen in Table 5, the work function of K_3SeBr is only 1.894 eV, and it is significantly lower than that of conventional photocatalysts, TiO_2 (4.13 eV), Na_3SBr (2.943 eV), ZnO (5.076 eV), and Na_3SI (3.1717 eV). Having such a low work function means that electrons can be easily released or transported from this material, resulting in more efficient charge separation. This reduces the recombination of the generated electron-hole pairs, which plays an important role in increasing the photocatalytic efficiency. Considering these properties, K_3SeBr appears to be a potential high-performance material in water splitting, solar cells, and various optoelectronic devices [122,123].

Table 5
The comparison of work function, ionization energy, electron affinity, and vacumm energy of K_3SeBr and related materials.

Structure	Vacumm energy (eV)	Work Function, ϕ (eV)	Electron affinity, χ (eV)	Ionization energy, IE (eV)	Reference
Na_3SI	5.089	3.1717	3.839	3.839	[27]
Na_3SBr	4.8380	2.943	3.57	3.57	[28]
K_3SeBr	4.528	1.894	3.665	3.665	**This work**
Cs_2TiI_6	-	-	4.98	6.06	[124, 125]
Cs_2TiBr_6	-		4.64	7.13	[124, 126]
WS_2		4.75	4.11	5.38	[127]
PEA_2SnI_4	-	4.67	2.98	5.15	[128]
TiO_2	-	4.13	-	-	[129]
ZnO	-	5.076	-	-	[130]

3.5.5. *Water redox potentials and bandage location of K_3SeBr anti-perovskite*

The valence band maximum (VBM) and conduction band minimum (CBM) with respect to the vacuum level were calculated using the following formula:

$$E_{CBM}(\text{Vacuum}) = -\chi - \frac{E_g}{2} \quad (24)$$

$$= -3.665 - \frac{1.7268}{2}$$

$$= -4.528 \text{ eV}$$

$$E_{VBM}(\text{Vacuum}) = -\chi + \frac{E_g}{2} \quad (25)$$

$$= -3.665 + \frac{1.7268}{2}$$

$$= -2.802 \text{ eV}$$

Here, Eg is the bandgap and χ is the electron affinity [131–135]. The relationship between the pH value and the water redox potentials is expressed by the following equations [131–136]:

$\text{HER} = -4.44 + \text{pH} \times 0.059$ eV for H^+/H_2

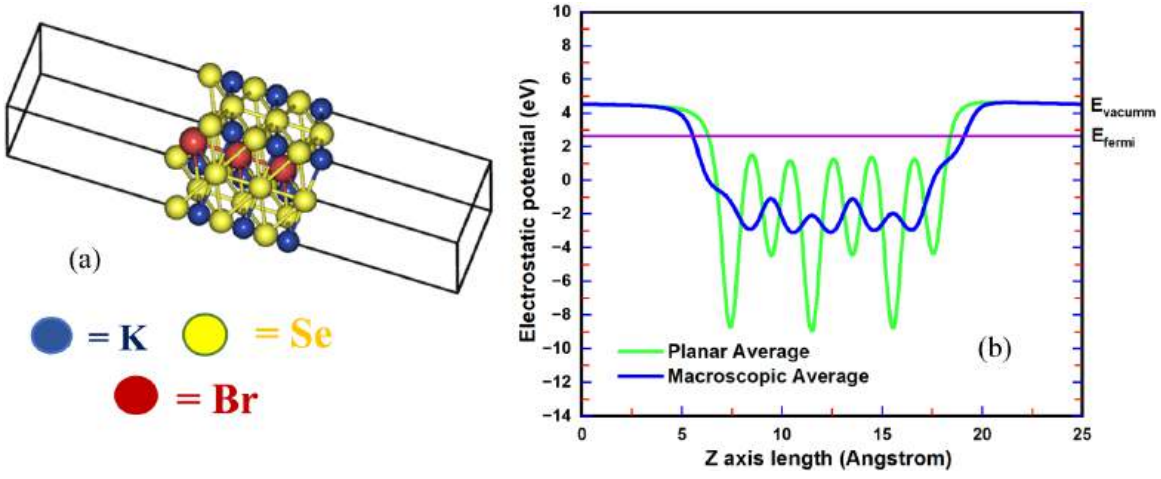

Fig. 5. K_3SeBr anti-perovskite compound: (a) Slab structure and (b) electrostatic potential.

OER = −5.67 + pH × 0.059 eV for O_2/H_2O
When pH = 7
HER = −4.03 eV for H^+/H_2
OER = −5.257 eV for O_2/H_2O
The VBM and CBM from vacuum level in the scale of NHE,
$^{NHE}E_{CBM}$ (Vacuum) = − 4.528 + 4.03 eV
= − 0.498 eV ($^{NHE}E_{CBM}$ (Vacuum) < 0 HER is possible [136])
$^{NHE}E_{VBM}$ (Vacuum) = − 2.802 + 5.257 eV
= 2.455 eV ($^{NHE}E_{VBM}$ (Vacuum) > 1.23 eV OER is possible [136])

In Fig. 6 is the band-edge location of the K_3SeBr anti-perovskite element and the redox potential of water at pH = 7. The analysis shows that the valence and conduction band edges of the material are consistent with the redox levels required for photocatalytic water splitting. This allows the production of hydrogen and oxygen using visible light. Notably, this compatibility makes K_3SeBr a potential anti-perovskite photocatalyst for green oxygen (O_2) and hydrogen (H_2) generation. Therefore, the compound also exhibits significant potential as a high-efficiency photocatalyst in STH energy production [131–136].

3.6. Optical characteristics of K_3SeBr anti-perovskite

The anti-perovskite and perovskite compounds are considered to have enormous potential in modern optoelectronic technologies due to their critical and unique optical features. When light interacts with such crystals, optical effects, such as absorption, reflection, dielectric function, penetration depth, refraction, energy loss function, and reflection, are clearly manifested. The present study reviews in detail various optical properties of K_3SeBr, such as reflectance, dielectric constant, refraction, extinction, electron energy loss, and other related parameters. Analysis of these properties has further highlighted its potential applications in applications, such as photocatalysis, optoelectronic devices, and photovoltaic [42,99,137–143].

3.6.1. Dielectric function of K_3SeBr anti-perovskite

The dielectric function ε(ω) is a fundamental indicator for analyzing the optical features of a material, which is essentially composed of two parts: one is real $\varepsilon_1(\omega)$, and the second is imaginary $\varepsilon_2(\omega)$ [144–148]. When light falls on a material, the values of these two components change a function of frequency (ω), clearly reflecting the reaction and energy absorption patterns of electrons within the material. The value of ε(ω) is usually determined using the Kramers-Kronig transformation [149], which establishes the fundamental relationship between the imaginary and real parts of the optical response. Notably, the imaginary component of the dielectric function, $\varepsilon_2(\omega)$, is a key indicator of the material electronic band structure. It reflects the photon energy needed to promote electrons from the valence band to the conduction band in the vicinity of the Fermi level, thereby offering essential insight into the material's effective bandgap. Typically, specific theoretical equations are used to determine the values of $\varepsilon_1(\omega)$, $\varepsilon_2(\omega)$, and ε(ω), which are useful in determining the light absorption capacity, energy level transition, and nature of optical activity of a material [144,145,149–151].

Dielectric function:

$$\varepsilon(\omega) = \varepsilon_1(\omega) + i\varepsilon_2(\omega) \tag{26}$$

Real part of dielectric function:

$$\varepsilon_1(\omega) = 1 + \frac{2}{\pi} P \int_0^{\infty} \frac{\varepsilon_2(\omega')\omega'}{\omega'^2 - \omega^2} d\omega \tag{27}$$

Imaginary part of dielectric function:

$$\varepsilon_2(\omega) = \frac{Ve^2}{2\pi\hbar m^2\omega^2} \int d^3K \sum | < \varphi_c|p|\varphi_v > |^2 \delta(E_c - E_v - \hbar\omega) \tag{28}$$

In Fig. 7(a) is the real part of dielectric function of K_3SeBr anti-perovskite. It can be seen that the value of $\varepsilon_1(\omega)$ rises gradually with increasing photon energy from 1 eV to 4 eV and achieves a peak value of about 2.25. However, after exceeding 5 eV, ε_1 suddenly drops rapidly to a negative value and takes a minimum value of about −0.14. This negative value of $\varepsilon_1(\omega)$ in the 5.3–6.8 eV energy range indicates that K_3SeBr exhibits a metal-like optical response in that region, which is mainly a result of plasma resonance. This resonance occurs due to the collective oscillation of valence electrons at high photon energies, which is typically seen in semiconductor materials with large bandgaps. Notably, this metallic response does not indicate true electrical conductivity; rather, it is a manifestation of plasmonic behavior, which causes powerful reflection and low transmission in a certain energy range. If the ε_1 value of a material is zero or negative, that material is suitable for exhibiting strong reflection or plasma resonance in that energy range, which is a critical feature in high-quality optical devices. On the other hand, in Fig. 7(b) is the imaginary part of the dielectric function $\varepsilon_2(\omega)$, which is mainly related to electron transition and light absorption from the valence to the conduction band. It can be seen that the value of ε_2 starts to increase rapidly from about 1.65 eV and achieves the highest value, i.e., about 2.35, at about 5.35 eV. The value then decreases rapidly, and, after about 8 eV, ε_2 drops to almost zero. This feature suggests that K_3SeBr absorbs most of the light in the photon energy range from 2 to 6.25 eV. This strong absorption in the visible-to-UV region establishes K_3SeBr as a highly promising element for use in high-efficient optical absorbers, photodetectors, and other light-dependent devices.

Although K_3SeBr is a semiconductor and has a direct bandgap of 1.726 eV, the negative value of $\varepsilon_1(\omega)$ at higher photon energies does not contradict its semiconducting nature. Rather, this negative $\varepsilon_1(\omega)$ value is

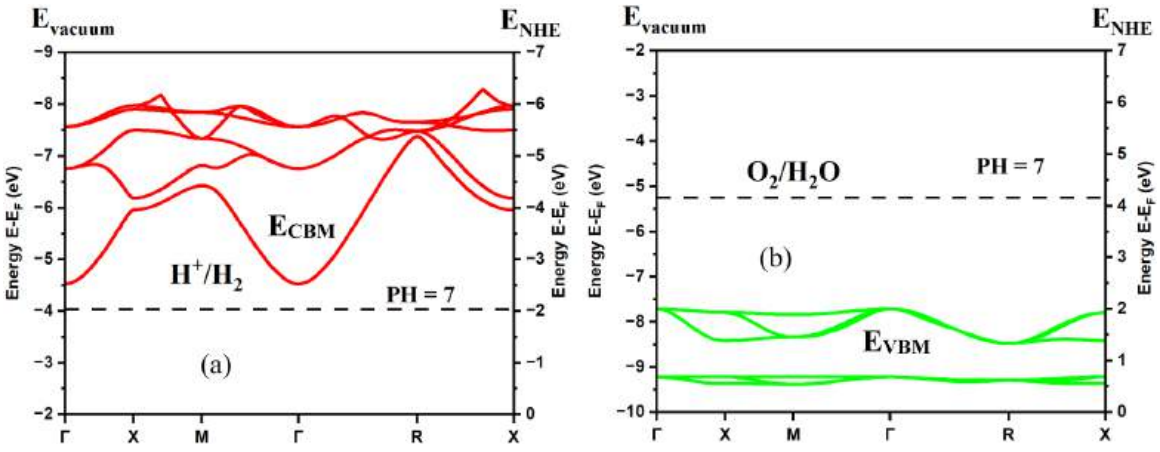

Fig. 6. The water redox potentials with bandage location (a) conduction and (b) valence band of K_3SeBr element.

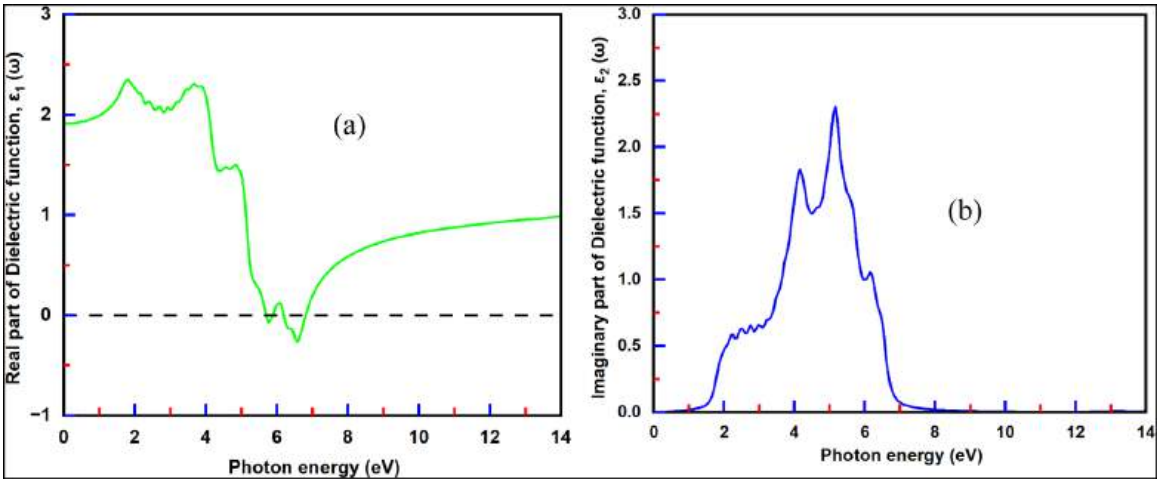

Fig. 7. The dielectric function of K_3SeBr anti-perovskite: (a) real part and (b) imaginary part.

a natural feature of wide-bandgap semiconductors, which occurs due to optical plasma resonance. This resonance is essentially the result of collective oscillations of valence electrons induced by high-energy photons, which enables the material to exhibit metal-like optical behavior in that energy region. However, the combination of a direct bandgap (1.7268 eV), powerful light absorption ability in the visible light wavelength region, and obvious plasmonic response at high photon energy proves that K_3SeBr can exhibit metal-like optical resonance even though it is a semiconductor. These properties together establish K_3SeBr as a highly promising element for use in visible wavelength light-dependent photocatalysis, solar-powered chemical reactions, and various optoelectronic devices.

A comparative picture of the optical properties of the compounds Na_3SI, Na_3SBr, K_3SeBr, Na_3OI, K_3OI and Ca_3AsX_3 (X = Br, I) can be clearly calculated from the different values of the dielectric function presented in Table 6. It is particularly noteworthy that the static dielectric constant of the K_3SeBr compound analyzed in this study is $\varepsilon_1(0) = 1.91$, which is relatively lower than most of the other compounds in the table. A low $\varepsilon_1(0)$ value indicates a low-level polarizability of the material, which is useful for fast-reacting optical materials. Similarly, the high-frequency dielectric constant $\varepsilon_1(\infty) = 0.98$, which is close to that of Na_3SI, Na_3OI, and K_3OI, shows that K_3SeBr exhibits a relatively stable optical response to high-energy photons. On the other hand, the initial critical point of $\varepsilon_2(\omega)$ is 1.65 eV, which is lower than that of most reported anti-perovskites. This means that K_3SeBr initiates interband transitions at relatively low photon energies, allowing it to participate more effectively in visible light absorption and optical excitation. Overall, the dielectric properties of K_3SeBr analyzed in this work establish it as a potential material for visible light-dependent optoelectronics, photocatalysis, and high-speed optical devices [144,145,149–151].

Table 6
The overview of dielectric function features of K_3SeBr anti-perovskite.

Structure	Static dielectric constant, $\varepsilon_1(0)$	High-frequency dielectric constant, $\varepsilon_1(\infty)$	Initial critical point location of, $\varepsilon_2(\omega)$ (eV)	Reference
Na_3SI	2.917	0.95	2.5	[27]
N_3SBr	2.62	0.78	2	[28]
K_3SeBr	1.91	0.98	1.65	This work
Na_3OI	2.62	0.94	2	[70]
K_3OI	2.34	0.96	1.05	[71]
Ca_3AsBr_3	4.75	1.65	1.97	[100]
Ca_3AsI_3	5.65	1.6	1.58	[100]

3.6.2. The effect of refraction, absorption, extinction, and reflection features of K_3SeBr anti-perovskite

It is very important to analyze the absorption, refraction, emission, and reflection properties of the K_3SeBr anti-perovskite material, as they clearly indicate how the material interacts with incident light or electromagnetic radiation. The absorption coefficient α(ω) indicates the amount of light absorbed per unit distance by the material, while the extinction coefficient k(ω) indicates how much the light becomes weak or attenuated, which is mainly a result of the absorption and re-emission processes [100,122]. On the other hand, reflection R(ω) is a process in which a portion of incident light hits the surface of a material and bounces back, while refraction n(ω) occurs when light changes speed and direction as it passes from one medium to another [55,60,152,153]. Accurate evaluation of these optical properties is crucial, as they can determine the potential of the K_3SeBr material for technological applications such as LEDs, optical coatings, solar cells, photocatalysis, sensors, fiber optics, thermal barrier coatings, and photodetectors. These optical reactions were analyzed in detail using specific equations to determine how light is absorbed, refracted, reflected, and emitted [55,60,100,122,152,153].

Absorption coefficient:

$$\alpha(\omega) = \frac{\sqrt{2}\omega}{c}\left[\sqrt{\varepsilon_1^2(\omega)+\varepsilon_2^2(\omega)} - \varepsilon_1(\omega)\right]^{\frac{1}{2}} \quad (29)$$

Extinction coefficient:

$$K(\omega) = \left[= \frac{\sqrt{\varepsilon_1^2(\omega)+\varepsilon_2^2(\omega)} - \varepsilon_1(\omega)}{2}\right]^{\frac{1}{2}} \quad (30)$$

Refractive index,

$$n(\omega) = \left[= \frac{\sqrt{\varepsilon_1^2(\omega)+\varepsilon_2^2(\omega)} + \varepsilon_1(\omega)}{2}\right]^{\frac{1}{2}} \quad (31)$$

Reflectivity,

$$R(\omega) = \frac{(n(\omega)-1)^2 + k^2}{(n(\omega)+1)^2 + K^2} \quad (32)$$

The light absorption α(ω) of the K_3SeBr inorganic anti-perovskite, as seen in Fig. 8(a), shows that the material starts absorbing light from around 180–200 nm (UV region). The light absorption in the visible wavelength region (380–700 nm) is around 0.5×10^5 cm^{-1}, indicating that the material is very responsive to visible light. However, the highest absorption ($\sim 5 \times 10^5$ cm^{-1}) occurs in the UV region at wavelengths of 180–300 nm. This clearly shows that the K_3SeBr material is highly active

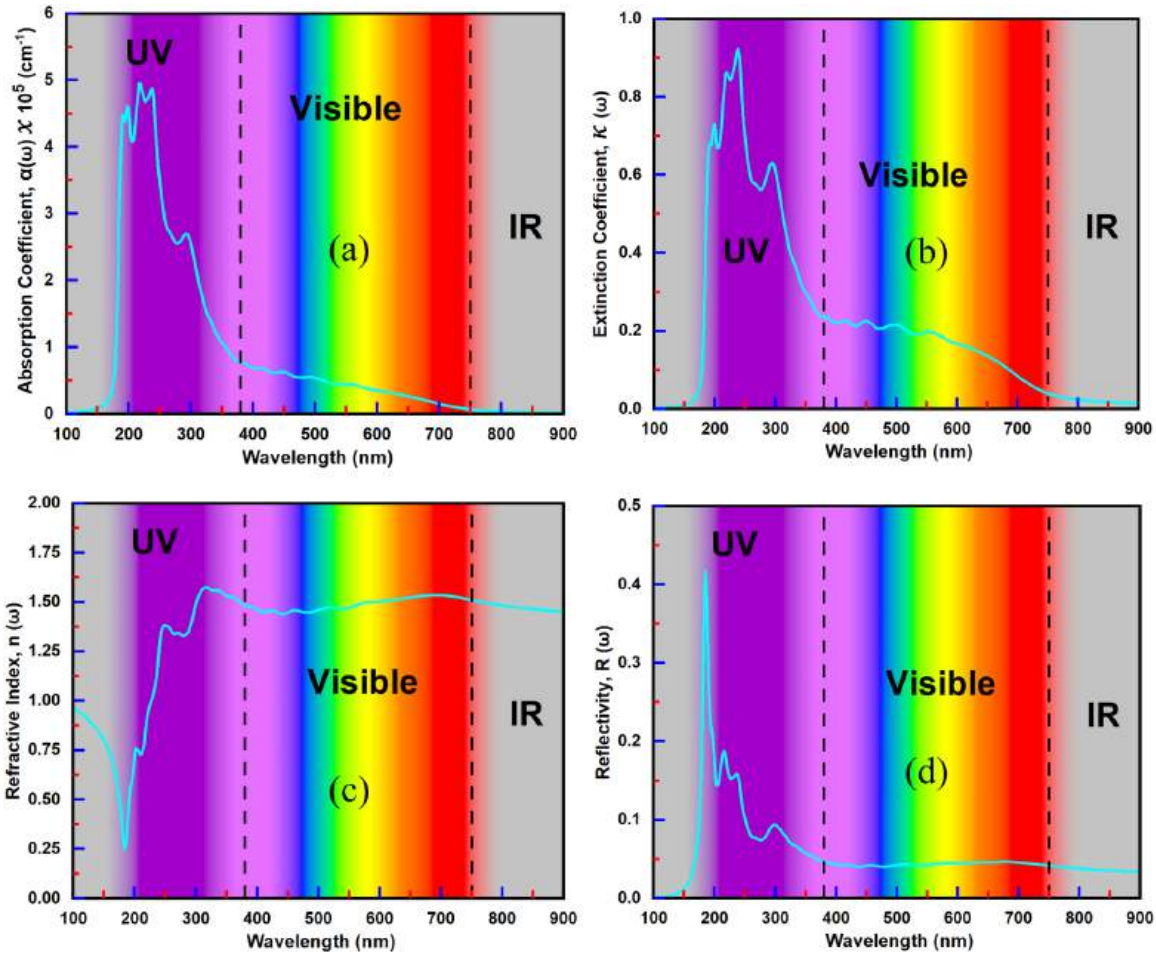

Fig. 8. (a) absorption, (b) extinction, (c) reflectivity, and (d) refraction of K_3SeBr anti-perovskite.

towards UV light but also has considerable absorption capacity in visible light. This behavior is useful for visible-light photocatalysis, photodetectors, and solar cells. Photocatalytic efficiency requires high α(ω), which facilitates light-driven electron excitation, which occurs efficiently in K_3SeBr.

According to Fig. 8(b), the k(ω) value increases gradually with wavelength from 150 to 250 nm and reaches a maximum value (~0.95) in the UV region (~240–260 nm). This indicates that the material is able to effectively absorb and attenuate UV light. In the visible light range, k (ω) is around 0.1–0.2, indicating moderate absorption, which is useful for optoelectronic and photocatalytic applications.

Next, Fig. 8(c) shows that the n(ω) increases gradually with wavelength from 180 to 335 nm. In the visible light region, n(ω) is around 1.5–1.55, indicating high refractive behavior. After 700 nm, the refractive index reduces, indicating a change in dielectric behavior. This characteristic is critical for photonic devices, optical lenses, waveguides, nonlinear optics, photovoltaics, and photocatalysis.

As seen in Fig. 8(d), the R(ω) value is the highest (~0.45) in the UV region (~200 nm). In the ultraviolet-to-visible-to-infrared light wavelength region (350–900 nm), the reflectivity is around 0.04–0.05, indicating low reflectivity. Low reflectivity means more light absorption, which increases the efficiency of photocatalytic and solar cell applications. On the other hand, high reflectivity in the UV and IR regions is useful for optical coating design.

In summary, the optical features of the K_3SeBr component indicate that it exhibits strong absorption, moderate extinction, a high refractive index, and low reflectivity in the UV to visible light wavelength range. These properties make K_3SeBr optimal for STH energy production, photocatalysis, photodetectors, LEDs, and other optoelectronic device applications. In particular, the combination of absorption and refractive behavior makes the material a promising candidate for dynamic optical devices and nonlinear optical applications [55,60,100,122,152–159].

3.6.3. The effect of energy loss, optical depth, and penetration depth characteristics of K_3SeBr anti-perovskite

In this study, three important photometric properties, optical depth, energy loss function (ELF), and penetration depth are studied in detail for analyzing the interaction of matter with light or radiation. Penetration depth essentially indicates how far light of a specific wavelength can penetrate a material, while optical depth indicates how much energy light loses as it passes through the material [160–162]. On the other hand, ELF analysis helps determine the amount of energy lost when light or electrons collide with the material and at what photon energy the probability of electron excitation is highest [163]. These three optical parameters play a very important role in the design of optoelectronic devices, solar cells, photocatalytic systems, radiation shielding, protective coatings, and fiber-optic technologies. To understand how and why energy is dissipated when light passes through the material, the analysis was performed using the following equations [160–163].

Penetration depth:

$$\delta(\omega) = \frac{1}{\alpha(\omega)} \tag{33}$$

Optical depth:

$$\tau(\omega) = \alpha(\omega) \times d \tag{34}$$

Energy loss function:

$$L(\omega) = \frac{\varepsilon_2(\omega)}{\varepsilon_1^2(\omega) + \varepsilon_2^2(\omega)} \quad (35)$$

Where the assumed medium thickness is d = 8 μm.

The penetration depth δ(ω) refers to how far light can penetrate a material. According to the analysis in Fig. 9(a), the penetration depth of K_3SeBr in the 100–650 nm wavelength region is very low, which proves that the material absorbs light very strongly in this range. However, as the wavelength increases, especially after 700 nm, the penetration depth gradually increases. This trend indicates that long wavelength or low energy light is able to penetrate relatively deeply into K_3SeBr, meaning that the material exhibits largely transparent behavior in this region.

Optical depth τ(ω) measures how much of the light entering a material is absorbed. It can be seen in Fig. 9(b) that the optical depth of the K_3SeBr material reaches about 400 in the wavelength range of 100–550 nm. This high value indicates that the material is capable of absorbing light very effectively in that wavelength region, especially in the visible and ultraviolet regions.

Also, the loss function L(ω) describes how much energy the electrons lose in the material. In Fig. 9(c), the highest peak is observed in the corresponding region of the wavelength of about 10 eV, indicating plasma resonance. It is related to the collective oscillation of electrons. The presence of this peak indicates metallic-like optical behavior of the material (photon energy equivalent to 8–10 eV) and strong electronic interactions.

K_3SeBr's remarkable ability to absorb visible-to-ultraviolet wavelength light, highest optical, and lowest penetration depth, make it critical for photocatalysis, UV detectors, photovoltaics, optical filters, and sensors. The material is able to rapidly absorb visible-to-ultraviolet light to produce photoelectrons, which is particularly critical in photocatalytic water-splitting processes such as the production of oxygen and hydrogen. Moreover, the ELF spectrum exhibits pronounced peaks around the plasma resonance region, suggesting that K_3SeBr may be a promising candidate for applications in electronic components as well as radiation-shielding technologies [154–163]. In addition, the key characteristics related to energy loss, optical depth, and penetration depth for the K_3SeBr compound are summarized in Table 7.

3.7. The energy band alignment profile, generation, and recombination of proposed four-semiconductor-layer structure

The primary objective of this study was to investigate the solar cell performance and STH production capability of the K_3SeBr element. To achieve this, an Al/FTO/SnS_2/K_3SeBr/CuO/Se device architecture was modeled and simulated utilizing SCAPS-1D, as shown in Fig. 10(a). The optoelectronic parameters of the constituent layers, FTO, SnS_2, K_3SeBr, and CuO, are summarized in Table 8. Also, Table 9 shows the interface features of the Al/FTO/SnS_2/K_3SeBr/CuO/Se single active absorber layer-based (K_3SeBr) proposed configuration. It can be seen from Fig. 10 (b) that the proposed Al/FTO/SnS_2/K_3SeBr/CuO/Se solar cell structure exhibits proper energy band alignment, which ensures efficient charge carrier transport. The FTO/SnS_2 interface has a low barrier for electron transport, with the conduction band offset being approximately 0 eV. On the other hand, the band offset at the K_3SeBr/CuO interface is about 0.476 eV, which creates a favorable path for hole transport. The K_3SeBr

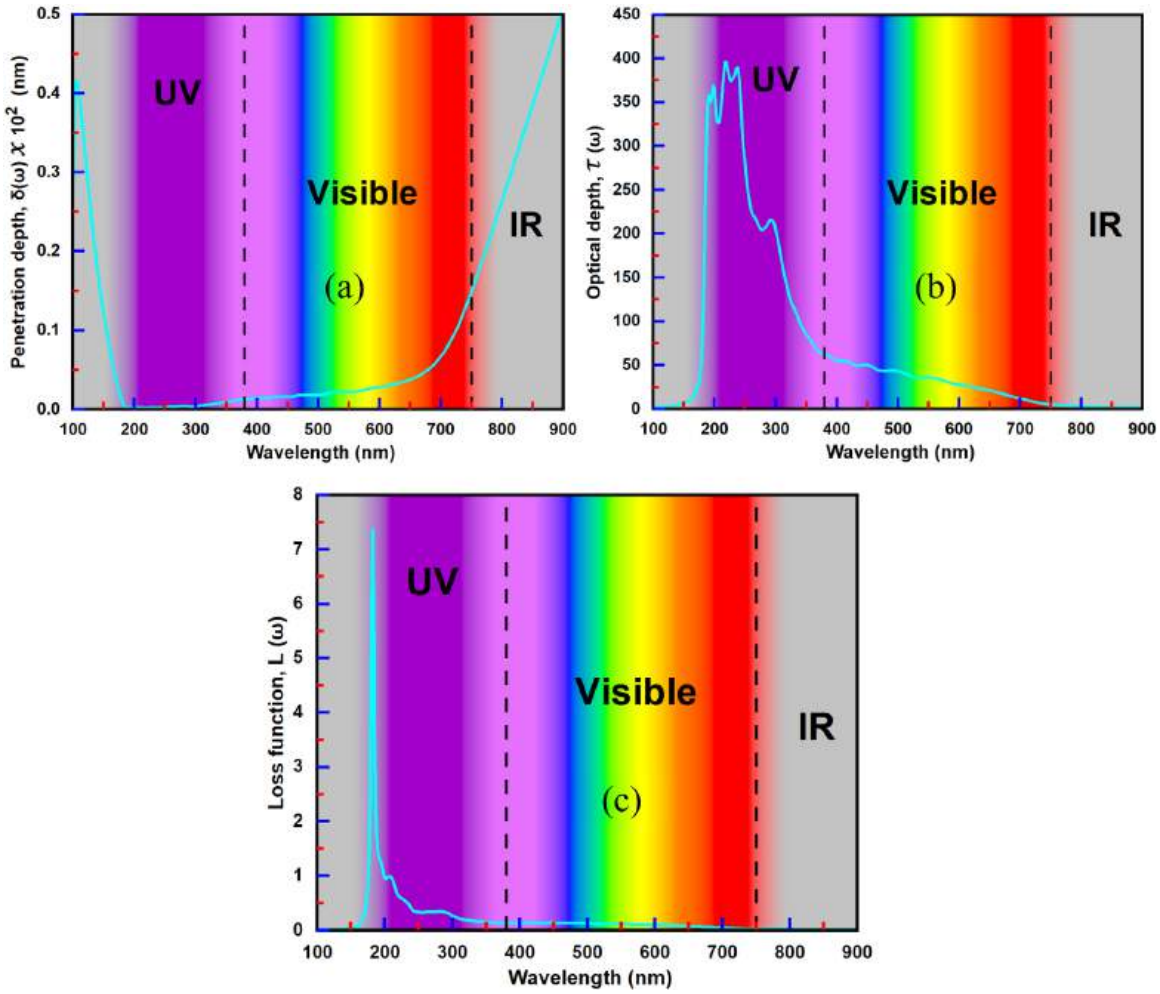

Fig. 9. (a) penetration depth, (b) optical depth, and (c) the energy loss function of K_3SeBr anti-perovskite.

Table 7
The overview of energy loss, optical depth, and penetration depth characteristics of K_3SeBr anti-perovskite.

Features	Features numerical quantity	Photon energy (eV) /wavelength (nm)	Remark
Maximum optical depth, $\tau_{max}(\omega)$	400	180 nm to 250 nm	Very high photon attenuation in deep-UV
Minimum optical depth, $\tau_{min}(\omega)$	50–40	400 nm to 900 nm	Low attenuation in visible-to-NIR, indicating partial transparency
Maximum penetration depth, $\delta_{max}(\omega)$	$(0.4–0.5)\times 10^2$	780 nm to 900 nm	Weak absorption in IR, material becomes more transparent
Minimum penetration depth, $\delta_{min}(\omega)$	2–5	200 nm to 700 nm	Strong absorption in UV-to-Visible, useful for photocatalysis and solar cell
Maximum energy loss function, $L_{max}(\omega)$	7.5	160–175 nm	Strong plasmon resonance collective electron oscillation
Minimum energy loss function, $L_{min}(\omega)$	0.05	300–900 nm	Minimal energy loss and stable propagation of photons/electrons

absorber layer has an electron affinity of −3.665 eV and an ionization potential of −3.665 eV, which provides a coherent band structure for the coordinated movement of electrons and holes. According to the energy band diagram, electrons flow easily from FTO to SnS_2 through K_3SeBr, and holes move in the opposite direction, ensuring effective charge separation and low recombination loss. This favorable band alignment strategically helps maintain the high fill factor (FF) and power conversion efficiency (PCE) of the device. Therefore, the K_3SeBr layer is considered an optoelectronically suitable and thermodynamically stable absorber, which is promising for high-efficiency anti-perovskite solar cell fabrication. Fig. 11(a) illustrates the carrier generation profile across the device thickness for the FTO/SnS_2/K_3SeBr/CuO structure. A high generation rate is observed near the front interface and within the K_3SeBr absorber layer, which gradually decreases with increasing thickness. This behavior is attributed to strong optical absorption near the illuminated side, where most photons are absorbed close to the SnS_2/K_3SeBr interface. The sustained generation throughout the 1.5 μm thick K_3SeBr layer confirms its effectiveness as the primary light-harvesting absorber. Fig. 11(b) presents the total recombination rate as a function of device thickness. The recombination is relatively low near the transport layers and increases within the bulk of the K_3SeBr absorber, where carrier density is higher. The recombination peak observed inside the absorber indicates bulk-dominated recombination rather than severe interface losses, suggesting favorable charge extraction at the SnS_2/K_3SeBr and K_3SeBr/CuO interfaces. Importantly, the overall recombination rate remains significantly lower than the generation rate across most of the absorber region, implying efficient carrier collection and limited recombination losses. These results demonstrate that the proposed device structure provides a suitable balance between carrier generation and recombination, supporting the potential of K_3SeBr as an efficient absorber material for optoelectronic applications.

3.8. Surface kinetics reaction and additional potential analysis of the proposed K_3SeBr anti-perovskite-based structure

In the proposed Al/FTO/SnS_2/K_3SeBr/CuO/Se structure, the surface reaction kinetics are mainly controlled by the favorable energy band alignment between the different layers. From the band diagram shown in Fig. 10(b), it can be seen that the conduction band offset at the FTO/

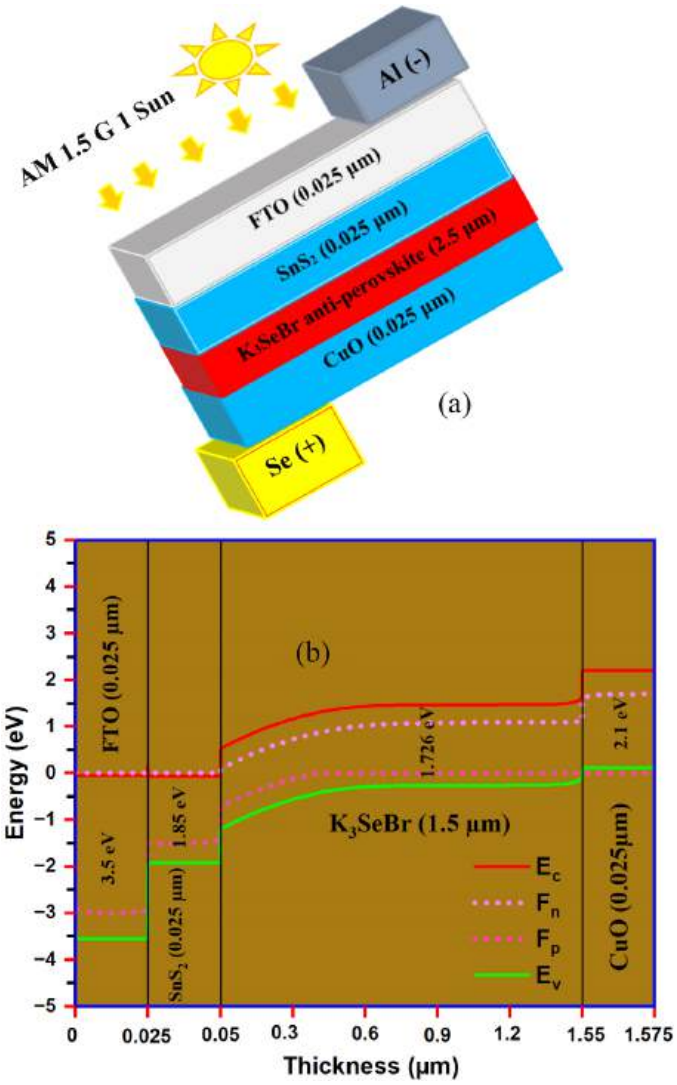

Fig. 10. (a) The proposed four-semiconductor-layer structure with a K_3SeBr active absorber layer for photovoltaics and photocatalysis and (b) Energy band alignment across the device thickness.

Table 8
The optoelectronic value of K_3SeBr active absorber with FTO, SnS_2, and CuO utilized in SCAPS-1D.

Parameter	FTO [28]	SnS_2 [28]	K_3SeBr (This work)	CuO [28]
W_{th} (cm)	0.025	0.025	1.5*	0.025
Eg (eV)	3.5	1.85	1.726	2.1
X_e (eV)	4	4.26	3.665	3.2
ε_r	9	17.7	1.91	7.11
N_{CB} (cm^{-3})	2.2×10^{18}	7.32×10^{18}	7.68×10^{18}	2.2×10^{18}
N_{VB} (cm^{-3})	1.8×10^{19}	1×10^{19}	2.5×10^{19}	1.8×10^{19}
V_{te} ($cm.s^{-1}$)	1×10^{7}	1×10^{7}	1×10^{7}	1×10^{7}
V_{th} ($cm.s^{-1}$)	1×10^{7}	1×10^{7}	1×10^{7}	1×10^{7}
μ_e ($cm^2/V.s$)	20	50	38.7	3.4
μ_h ($cm^2/V.s$)	10	25	8.17	3.4
N_D (cm^{-3})	2E+ 19	9.85E+ 19	0	0
N_A (cm^{-3})	0	0	1E+ 15*	1E+ 20
N_t (cm^{-3})	1×10^{15}	1×10^{14}	1×10^{15}*	1×10^{15}
Absorption data (1/m)			ABSDF	

* Variable domain was used for initial investigation. ABSDF refers to the absorption file-related data of K_3SeBr element. This absorption data file is taken from the absorption graph shown in Fig. 8(a).

Table 9
The recommended structure interface features.

Parameter	SnS_2/K_3SeBr and K_3SeBr/CuO
Defect type	Neutral
Hole and electron cross-section area (cm^2)	1E-19
Energetic distribution	Single
Energy level E_t	Above the highest Ev
Reference Energy E_r (eV)	0.600
Total density (cm^{-3})	1E+ 10

SnS_2 interface is almost zero, which creates a low barrier for electron injection. Similarly, the favorable valence band offset at the K_3SeBr/CuO interface facilitates hole transport. These favorable band offsets ensure efficient charge transfer at the interface, which can be considered as an improved reflection of the surface reaction kinetics. In addition, the band bending and built-in electric field between the absorber and transport layers act as an additional driving potential, which drives the photo-generated electrons and holes in opposite directions and further strengthens the charge separation. This additional potential helps to reduce charge carrier accumulation and reduce recombination. Analysis of the generation and recombination profiles (Fig. 11) shows that recombination is mainly confined to the absorber bulk, and no strong recombination is observed at the interface. Such behavior indicates that charge transport at the surface is efficient and interfacial losses are relatively low. As a result, the proposed device structure has improved surface charge kinetics, sufficient built-in potential, and limited recombination loss, which ensures overall high photovoltaic and STH performance.

3.9. The current-voltage (J-V) and wavelength vs. external quantum efficiency of the proposed K_3SeBr anti-perovskite-structure

The photoelectric output of the proposed structure with previous published work, presented in Table 10, reveals outstanding device performance. The optimized cell delivered a J_{sc} of 29.369 mA/cm^2, an V_o of 1.1648 V, a FF of 82.0 %, and a PCE of 28.02 %. These results clearly highlight the excellent photovoltaic characteristics of the designed device. The J–V curve in Fig. 12(a) shows that the structure achieves slightly higher J_{sc} along with a notably elevated V_o, indicating that K_3SeBr contributes effectively to enhancing both current generation and voltage output. Meanwhile, the EQE spectrum in Fig. 12(b) shows a peak external quantum efficiency of 99.98 % within the 350–700 nm wavelength range, confirming the strong light-harvesting ability of the device.

3.10. The theoretically computation of STH production efficiency

Knowing the STH efficiency is crucial, as it determines how much energy an element or absorber layer can produce from sunlight directly into hydrogen power generation. That is, STH production efficiency shows how effectively the material is actually able to produce hydrogen. This indicator is extremely critical for new element design and modeling, comparative analysis, and evaluating the potential of photocatalysis or PEC devices. In this study, the nessesary formulas were used to determine the STH energy production efficiency of the K_3SeBr element [156–160].

$$\eta_{STH}(\%) = \frac{J_{op}(A/cm^2).\quad 1.23\quad (V).\qquad \eta_F}{P_{in}\quad (W/cm^2)} \times 100 \tag{36}$$

This research utilized AM_1.5 G quality 1 Sun illumination conditions. In SCAPS-1D simulations, the J_{sc} for K_3SeBr anti-perovskite was found to be 29.363 mA/cm^2. The maximum current that the cell delivers during hydrogen generation in an unbiased PEC or photocatalytic cell is generally considered to be the short-circuit current (J_{sc}). That is why J_{sc} can be taken as the operating current (J_{op}) in theoretical calculations or simulation-based analysis. This simplifies the process of determining STH production efficiency and also allows straightforward comparative analysis with other elements or structures [167–173].

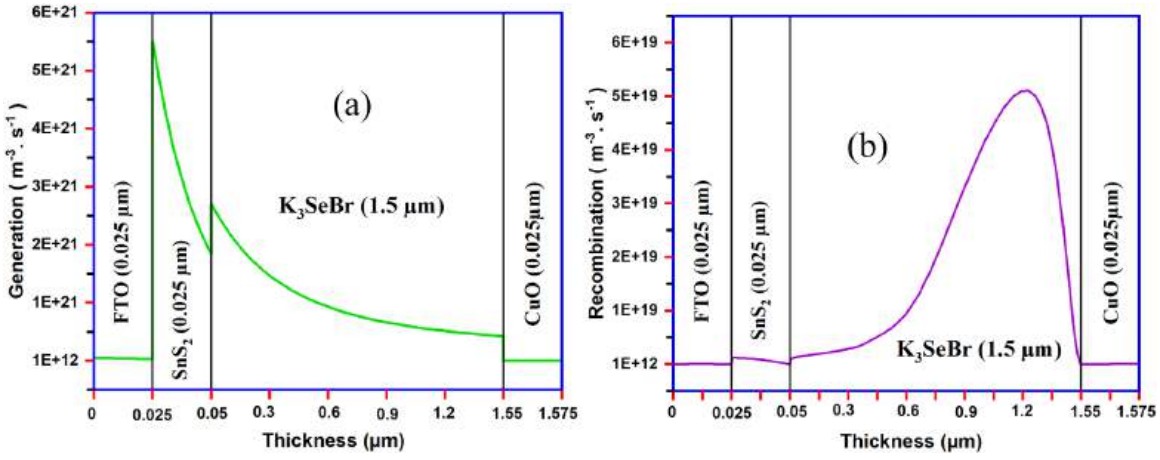

Fig. 11. (a) The generation and (b) the total recombination profile across the device thickness for the proposed four-semiconductor-layer structure with a K_3SeBr active absorber.

Table 10
The comparison of photovoltaic features of the K_3SeBr anti-perovskite with published work.

Structure	V_o (Volts)	PCE (%)	J_{sc} (mA/cm^2)	FF (%)	Reference
Al/FTO/SnS_2/K_3SeBr/CuO/Se	1.1648	28.02	29.363	82.0	**This work**
Ag/FTO/SnS_2/Sr_3AsI_3/Ni	0.913	28	35.75	86.26	[100]
FTO/SnS_2/Ca_3AsI_3/CuO/Au	1.2046	28.22	26.14	89.61	[164]
Al/FTO/SnS_2/Na_3SBr/CuO/Au	1.544	27.172	20.82	84.51	[28]
AZO/TiO_2/$CsPbI_3$/$RbGeI_3$/Ni	1.04	31.91	34.77	88.38	[165]
Al/Na_3SI/Se	1.6851	40.11	26.189	90.88	[27]
SnS_2/$CsSn_{0.5}Ge_{0.5}I_3$/$FASnI_3$/Zn_3P_2/Pt	1.185	33.16	31.218	89.58	[166]

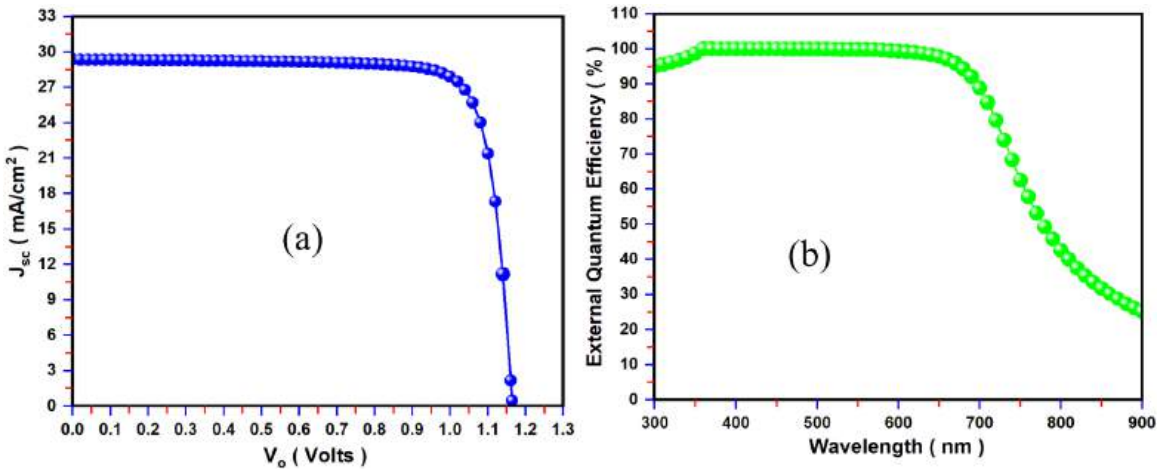

Fig. 12. The recommended solar cell structure: (a) J-V and (b) external quantum efficiency (EQE) spectra features.

In this case, $J_{Sc} = J_{op} = 29.363$ mA/cm^2 $= 0.029363$ A/cm^2
and $P_{in} = 1000$ W/m^2 $= 0.1$ W/cm^2

In several previous studies, many authors conventionally considered the value of η_F to be 1.0 without further refinement. However, in the present work, we deliberately selected $\eta_F = 0.8$ to achieve a more realistic description of the physical behavior of the system. This slightly reduced value allows the computed parameters to better approximate the trends observed in experimental measurements, thereby enhancing the reliability and accuracy of our theoretical predictions.

η_{STH} (%) = 28.89%

The computational analysis shows that a single anti-perovskite-based structure, Al/FTO/SnS_2/K_3SeBr/CuO/Se, is capable of delivering an STH energy production efficiency of over 28 %. If 0.8 Faradic efficiency is assumed, this value comes near to actual experimental results, which is considered a more reliable indicator for evaluating the performance of the element [167–173]. Although this study is purely theoretical, previous successes in the anti-perovskite class support the feasibility of K_3SeBr. For example, Na_3OX (X = Cl, Br, I, BH_4) anti-perovskites have been successfully characterized and synthesized by mechanochemical methods, confirming the practical applicability of sodium-based anti--perovskites [172]. Similarly, anti-perovskites of the Ca_3MN (M = As, P, Sb, Ge, Bi, Pb, and Sn) type have also been synthesized in the laboratory, and their stability and repeatability have been demonstrated [173]. Furthermore, the definition and characterization of Mg_3AsN anti-perovskites are also presented, which further strengthens the possibility of experimental implementation of similar compounds of this class [174]. This research clearly shows that the synthesis of K_3SeBr is feasible, providing a strong basis for future experimental verification. Although K_3SeBr shows excellent thermodynamic and mechanical stability (phonon stability, elastic constants, and formation energy), it should be noted that Se and Br have some toxicity, and halide-based materials may degrade under humid or ambient conditions. Proper encapsulation or protective layers may be required for practical applications.

4. Conclusions

In this research, the structural, dynamic, optical, mechanical, electronic, and photocatalytic features of K_3SeBr anti-perovskite compounds have been analyzed in detail utilizing DFT-based (GGA-PBE) methods. The phonon dispersion analysis after structural optimization showed that the compound is dynamically stable, indicating its potential for practical applications. According to the elastic constants and mechanical analysis, K_3SeBr is mechanically stable, as well as sufficiently strong and ductile (B/G ≈ 1.923), which indicates tolerance against stress and tension and technical durability. According to the electronic properties, the compound is a direct bandgap ((1.726 eV, PBE) and (2.576 eV, HSE06)) semiconductor, and the band edges (VBM and CBM) are compatible with the redox potential required for sunlight-to-hydrogen production via photocatalytic water splitting. Optical analysis has shown that K_3SeBr is capable of strong absorption from UV to visible light ($\alpha \approx (5–0.5) \times 10^5$ cm^{-1}), making it highly effective for solar cells and photocatalysis. The extinction coefficient (k ≈ 0.1–0.95) and refractive index (n ≈ 1.5–1.55) indicate that the compound can transmit and reflect light effectively, and a low refractive index of R ≈ 0.04–0.45 is suitable for absorbing visible light. Penetration depth (δ ≈ 2–5 nm) and optical depth (τ ≈ 40–400) analysis show that the compound has strong absorption in the visible–ultraviolet light wavelength region. The energy loss function ($L_{max} \approx 7.5$) indicates plasmonic resonance in the UV region, which proves the metal-like optical behavior and strong electronic interactions of the compound. The results of the proposed Al/FTO/SnS_2/K_3SeBr/CuO/Se solar cell structure in SCAPS-1D simulations: $J_{sc} = 29.369$ mA/cm^2, $V_o = 1.1648$ V, FF = 82 %, PCE = 28.02 %, and solar-to-hydrogen (STH) efficiency ≈ 28.89 % ($\eta F = 0.8$). These results demonstrate that K_3SeBr is highly efficient in visible–UV light and is promising for hydrogen production from solar energy. In summary, the K_3SeBr anti-perovskite compound is structurally stable, mechanically strong, and ductile, with high absorption capacity and significant refraction, exhibiting strong STH efficiency. These properties make it a potential material for photocatalysis, hydrogen production from solar energy, optoelectronic devices, and sustainable renewable energy technologies. Also, the successful experimental implementation of other anti-perovskites, as compared with Tables 11 and 12, further strongly supports the feasibility of experimental preparation and usability of

Table 11
The comparison of STH conversion efficiency of the recommended structure with published works.

Photocatalysis structure	Simulated/ Experimental	η_{STH} (%)	Reference
InGaP/GaAs/Ge	Experimental	24.4	[6]
GaInP/GaInAs/Ge	Simulated	35.25	[8]
$(MAPb(I_{0.85}Br_{0.15})_3)$/Si	Experimental	17.52	[10]
CZTS/CdS/TiO_2/Pt	Experimental	9.91	[12]
AlGaAs/Si RuO_2/Pt_{black}	Experimental	18.3	[21]
$GaInP_2$/GaAs	Experimental	12.4	[24]
Al/Na_3SI/Se	Simulated	25.769	[27]
Al/FTO/SnS_2/K_3SeBr/CuO/ Se	Simulated	28.89	This work
PMA_2PbI_4/MoS_2	Experimental	2.07	[175]
$CsPbBr_3$	Simulated	12	[176]

Table 12
The comparison of dynamic, mechanical, and optoelectronic properties of the K_3SeBr element with previous works.

Structure	$MAPBI_3$	$FASnI_3$	Cs_2SnI_6	$MASnI_3$	K_3OI	Na_3SI	Na_3SBr	K_3SeBr
Bandgap (eV)	1.55	4.2	1.42	1.3	1.03	2.499	2.5361	1.726
Electron affinity (eV)	3.9	1.45	4.07	4.2	-	3.893	3.57	3.665
Dielectric constant, $\varepsilon_1(0)$	30	8.2	7.2	8.2	2.34	2.917	2.62	1.91
Light absorption capability (cm^{-1})	(1×10^5) visible region	(1×10^5) visible region	($>10^5$) visible region	(1×10^5) visible region	(1.1×10^4) visible region	(13×10^5–0.5×10^5) in the UV-to-visible region	(13×10^5–0.5×10^5) in the UV-to-visible-to-NIR region	(5×10^5–0.5×10^5) in the UV-to-visible region
Mobility of hole, μ_e (cm^2/Vs)	2.2	22	9	1.6	-	7.56	31.23	8.17
Mobility of electron, μ_e (cm^2/Vs)	2.2	22	5.11	1.6	-	63.18	55.16	38.7
Phonon stability	Stable	Stable	Stable	Stable	Stable	Stable	Stable	Stable
Mechanical stability	Stable	Stable	Stable	Stable	Stable	Stable	Stable	Stable
Pugh's ratio	2.39 (ductile)	2.55 (ductile)	1.92 (ductile)	2.27 (ductile)	1.31 (brittle)	1.638 (brittle)	1.81 (ductile)	1.923 (ductile)
Application	Solar cell	Solar cell	Optrical, electronic, and solar cell	Solar cell	Photo-catalysis, opto-electronic, and solar cell	Photo-catalysis, opto-electronic, and solar cell	Photo-catalysis, opto-electronic, and solar cell	Photo-catalysis, opto-electronic, and solar cell
Reference	[177] [178] [179]	[180] [181] [182]	[183] [184] [185]	[186] [187]	[188]	[27]	[28]	**This work**

K_3SeBr, which provides an important foundation for future research and applications.

CRediT authorship contribution statement

Md. Earshad Ali: Data curation, Conceptualization, Formal analysis, Methodology, Investigation, Project administration, Resources, Software, Validation, Visualization, Writing – original draft, Writing – review & editing, Supervision. **Karim Kriaa:** Conceptualization, Formal analysis, Data curation, Investigation, Resources, Software, Validation, Visualization, Writing – original draft, Writing – review & editing, Funding acquisition. **Md. Nobiul Islam:** Investigation, Conceptualization, Formal analysis, Data curation, Resources, Software, Visualization, Methodology, Writing – original draft, Writing – review & editing. **Md. Shizer Rahman:** Formal analysis, Investigation, Resources, Writing – review & editing, Software, Visualization, Writing – original draft, Supervision. **Noureddine Elboughdiri:** Formal analysis, Investigation, Writing – review and editing, Resources, Software, Visualization, Writing – original draft. **Md. Azizur Rahman:** Formal analysis, Investigation, Resources, Software, Visualization, Writing – review & editing. **Mohamed Benghanem:** Methodology, Formal analysis, Investigation, Funding acquisition, Writing – original draft, Visualization, Writing – review & editing.

Ethical approval

The authors declare that this research does not involve study on human subjects, human components, tissues, or organisms.

Declaration of Competing Interest

The authors declare that they have no known competing financial interests or personal relationships that could have appeared to influence the work reported in this paper.

Acknowledgment

The researchers wish to extend their sincere gratitude to the Deanship of Scientific Research at the Islamic University of Madinah (KSA) for the support provided to the Post-Publishing Program. Also, we are sincerely grateful to the creators of Quantum ESPRESSO and SCAPS-1D software; without their advanced tools, the computational analysis of this study would not have been possible.

Data availability

Data will be provided upon request.

References

[1] M.K. Masood, et al., Theoretical investigation of XSnH3 (X: Rb, Cs, and Fr) perovskite hydrides for hydrogen storage application, Int. J. Hydrog. Energy 63 (Apr. 2024) 1248–1257, https://doi.org/10.1016/j.ijhydene.2024.03.229.
[2] T. Li, N. Tsubaki, Z. Jin, S-scheme heterojunction in photocatalytic hydrogen production, J. Mater. Sci. Technol. 169 (Jan. 2024) 82–104, https://doi.org/10.1016/j.jmst.2023.04.049.
[3] X. Song, H. Bu, Y. Fan, J. Wang, M. Zhao, Photocatalytic hydrogen production and storage in carbon nanotubes: a first-principles study, RSC Adv. 12 (27) (2022) 17029–17035, https://doi.org/10.1039/D2RA02349K.
[4] J. Jayaprabakar, et al., Nano materials for green hydrogen production: technical insights on nano material selection, properties, production routes and commercial applications, Int J. Hydrog. Energy 52 (Jan. 2024) 674–686, https://doi.org/10.1016/j.ijhydene.2023.06.109.
[5] S. Bimli, et al., Perovskite BaSnO3 nanoparticles for solar-driven bi-functional photocatalytic activity: PEC water splitting and Wastewater treatment, Int J. Hydrog. Energy 51 (Jan. 2024) 1497–1507, https://doi.org/10.1016/j.ijhydene.2023.11.163.
[6] A. Nakamura, et al., A 24.4% solar to hydrogen energy conversion efficiency by combining concentrator photovoltaic modules and electrochemical cells, Appl. Phys. Express 8 (10) (Oct. 2015) 107101, https://doi.org/10.7567/APEX.8.107101.
[7] S.F. Ahmed, et al., Carbon-based nanomaterials: characteristics, dimensions, advances and challenges in enhancing photocatalytic hydrogen production, Int J. Hydrog. Energy 52 (Jan. 2024) 424–442, https://doi.org/10.1016/j.ijhydene.2023.03.185.
[8] C. Kale, H. Esen, High-efficiency solar-to-hydrogen systems: multi-junction CPV cell coupled with solid oxide electrolyzer, Int J. Hydrog. Energy 143 (Jul. 2025) 1255–1266, https://doi.org/10.1016/j.ijhydene.2025.01.286.

[9] V.-H. Dang, T.-A. Nguyen, M.-V. Le, D.Q. Nguyen, Y.H. Wang, J.C.-S. Wu, Photocatalytic hydrogen production from seawater splitting: current status, challenges, strategies and prospective applications, Chem. Eng. J. 484 (Mar. 2024) 149213, https://doi.org/10.1016/j.cej.2024.149213.

[10] H. Park, et al., Water splitting exceeding 17% solar-to-hydrogen conversion efficiency using solution-processed Ni-based electrocatalysts and perovskite/Si Tandem solar cell, ACS Appl. Mater. Interfaces 11 (37) (Sep. 2019) 33835–33843, https://doi.org/10.1021/acsami.9b09344.

[11] R. Li, et al., Engineering of bimetallic Au–Pd alloyed particles on nitrogen defects riched g-C3N4 for efficient photocatalytic hydrogen production, Int J. Hydrog. Energy 63 (Apr. 2024) 1116–1127, https://doi.org/10.1016/j.ijhydene.2024.03.113.

[12] M. Abbas, et al., Highest solar-to-hydrogen conversion efficiency in Cu2ZnSnS4 photocathodes and its directly unbiased solar seawater splitting, Nanomicro Lett. 17 (1) (Dec. 2025) 257, https://doi.org/10.1007/s40820-025-01755-8.

[13] L. Gao, K. Hao, F. Yang, P. Hu, D. Li, Research on the effect of two-dimensional perovskite crystal structures on photocatalytic hydrogen production, Mater. Lett. 371 (Sep. 2024) 136967, https://doi.org/10.1016/j.matlet.2024.136967.

[14] H. Bian, D. Li, J. Yan, S. (Frank) Liu, Perovskite – A wonder catalyst for solar hydrogen production, J. Energy Chem. 57 (Jun. 2021) 325–340, https://doi.org/10.1016/j.jechem.2020.08.057.

[15] Q. Liu, et al., Cobalt@nitrogen-doped bamboo-structured carbon nanotube to boost photocatalytic hydrogen evolution on carbon nitride, Appl. Catal. B 254 (Oct. 2019) 443–451, https://doi.org/10.1016/j.apcatb.2019.04.098.

[16] S. Menia, D. Fetta, M. Belacel, M. Benlembarek, Photocatalytic Hydrogen Production From TiO2, Islam. Univ. J. Appl. Sci. (2026) 101–112, https://doi.org/10.63070/jesc.2025.044.

[17] H. Bian, et al., Graded bandgap CsPbI2+Br1− perovskite solar cells with a stabilized efficiency of 14.4%, Joule 2 (8) (Aug. 2018) 1500–1510, https://doi.org/10.1016/j.joule.2018.04.012.

[18] S. Patial, V. Hasija, P. Raizada, P. Singh, A.A.P. Khan Singh, A.M. Asiri, Tunable photocatalytic activity of SrTiO3 for water splitting: strategies and future scenario, J. Environ. Chem. Eng. 8 (3) (Jun. 2020) 103791, https://doi.org/10.1016/j.jece.2020.103791.

[19] T. Chen, et al., Room temperature synthesized BaTiO3 for photocatalytic hydrogen evolution, J. Alloy. Compd. 754 (Jul. 2018) 184–189, https://doi.org/10.1016/j.jallcom.2018.04.300.

[20] M.M. Parvaiz, A. Khalil, H.I. Elsaeedy, M.B. Tahir, S. Ayub, Z. Ullah, Extensive screening of novel BaXH3 (X = V, Cr, Co, Ni, Cu, and Zn) perovskites for physical properties and hydrogen storage application: a DFT study, Int J. Hydrog. Energy 87 (Oct. 2024) 1056–1073, https://doi.org/10.1016/j.ijhydene.2024.09.113.

[21] S. Licht, Over 18% solar energy conversion to generation of hydrogen fuel; theory and experiment for efficient solar water splitting, Int J. Hydrog. Energy 26 (7) (Jul. 2001) 653–659, https://doi.org/10.1016/S0360-3199(00)00133-6.

[22] N. Xu, et al., First-principles investigations for the hydrogen storage properties of XVH3 (X=Na, K, Rb, Cs) perovskite type hydrides, J. Mater. Res. Technol. 26 (Sep. 2023) 4825–4834, https://doi.org/10.1016/j.jmrt.2023.08.218.

[23] N. Xu, Y. Chen, S. Chen, S. Li, W. Zhang, First-principles investigation for the hydrogen storage properties of XTiH3 (X=K, Rb, Cs) perovskite type hydrides, Int J. Hydrog. Energy 50 (Jan. 2024) 114–122, https://doi.org/10.1016/j.ijhydene.2023.06.254.

[24] J.L. Young, K.X. Steirer, M.J. Dzara, J.A. Turner, T.G. Deutsch, Remarkable stability of unmodified GaAs photocathodes during hydrogen evolution in acidic electrolyte, J. Mater. Chem. A Mater. 4 (8) (2016) 2831–2836, https://doi.org/10.1039/C5TA07648J.

[25] J. Wu, T. Wu, Ensure access to affordable, reliable, sustainable and modern energy for all, UN Chron. 51 (4) (Jun. 2015) 17–18, https://doi.org/10.18356/24ef28d2-en.

[26] A. Rogalski, F. Wang, J. Wang, P. Martyniuk, W. Hu, The perovskite optoelectronic devices – a look at the future, Small Methods 9 (1) (Jan. 2025), https://doi.org/10.1002/smtd.202400709.

[27] Md.E. Ali, First-principles investigation of the structural, electronic, and optical properties of a novel Na3SI anti-perovskite for efficient solar-to-hydrogen energy conversion via photocatalytic water splitting, Int J. Hydrog. Energy 194 (Dec. 2025) 152217, https://doi.org/10.1016/j.ijhydene.2025.152217.

[28] Md.E. Ali, DFT-based investigation of optoelectronic, dynamic, thermodynamic, mechanical, and strain-engineered properties of a novel lead-free Na3SBr inorganic anti-perovskite and achieving over 27% solar cell efficiency, J. Alloy. Compd. 1043 (Oct. 2025) 184221, https://doi.org/10.1016/j.jallcom.2025.184221.

[29] G. Ji, et al., B-site columnar-ordered halide double perovskites: theoretical design and experimental verification, J. Am. Chem. Soc. 143 (27) (Jul. 2021) 10275–10281, https://doi.org/10.1021/jacs.1c03825.

[30] Z. Liu, et al., Bandgap engineering and thermodynamic stability of oxyhalide and chalcohalide antiperovskites, Ceram. Int 47 (23) (Dec. 2021) 32634–32640, https://doi.org/10.1016/j.ceramint.2021.08.159.

[31] O. Benguerine, Z. Nabi, A. Hachilif, B. Bouabdallah, B. Benichou, Bright future in optoelectronics, photovoltaics and thermoelectric using the double perovskites oxides BaSrMgB'O6 (B'=Te, W), Comput. Condens. Matter 30 (Mar. 2022) e00649, https://doi.org/10.1016/j.cocom.2022.e00649.

[32] X. Li, Y. Zhang, W. Kang, Z. Yan, Y. Shen, J. Huo, Anti-perovskite nitrides and oxides: properties and preparation, Comput. Mater. Sci. 225 (Jun. 2023) 112188, https://doi.org/10.1016/j.commatsci.2023.112188.

[33] Y. Wang, et al., Antiperovskites with exceptional functionalities, Adv. Mater. 32 (7) (Feb. 2020), https://doi.org/10.1002/adma.201905007.

[34] M.Y. Chern, D.A. Vennos, F.J. Disalvo, Synthesis, structure, and properties of anti-perovskite nitrides Ca3MN, M=P, As, Sb, Bi, Ge, Sn, and Pb, J. Solid State Chem. 96 (2) (Feb. 1992) 415–425, https://doi.org/10.1016/S0022-4596(05)80276-2.

[35] G. Tang, et al., Designing antiperovskite derivatives *via* atomic-position splitting for photovoltaic applications, Mater. Horiz. 11 (21) (2024) 5320–5330, https://doi.org/10.1039/D4MH00526K.

[36] H. Zhong, et al., Structure–composition–property relationships in antiperovskite nitrides: guiding a rational alloy design, ACS Appl. Mater. Interfaces 13 (41) (Oct. 2021) 48516–48524, https://doi.org/10.1021/acsami.1c10137.

[37] D. Kalita, P. Sahu, U. Manju, Anti-perovskites for photovoltaics: materials development and challenges, J. Phys. D. Appl. Phys. 57 (34) (Aug. 2024) 343002, https://doi.org/10.1088/1361-6463/ad4daf.

[38] S.A. Khandy, I. Islam, A. Laref, M. Gogolin, A.K. Hafiz, A.M. Siddiqui, Electronic structure, thermomechanical and phonon properties of inverse perovskite oxide (Na3OCl): an ab initio study, Int J. Energy Res 44 (4) (Mar. 2020) 2594–2603, https://doi.org/10.1002/er.4982.

[39] K.T. Lai, I. Antonyshyn, Y. Prots, M. Valldor, Anti -perovskite Li-battery cathode materials, J. Am. Chem. Soc. 139 (28) (Jul. 2017) 9645–9649, https://doi.org/10.1021/jacs.7b04444.

[40] G.S.H. Thien, et al., Recent advances in halide perovskite resistive switching memory devices: a transformation from lead-based to lead-free perovskites, ACS Omega 7 (44) (Nov. 2022) 39472–39481, https://doi.org/10.1021/acsomega.2c03206.

[41] U. Rani, et al., Electronic structure, theoretical power conversion efficiency, and thermoelectric properties of bismuth-based alkaline earth antiperovskites, J. Mol. Model 29 (10) (Oct. 2023) 329, https://doi.org/10.1007/s00894-023-05732-z.

[42] A. Meziany, et al., Toward lightweight solid-state hydrogen storage: computational investigation of potassium antiperovskites, Phys. Status Solidi (a) (Jun. 2025), https://doi.org/10.1002/pssa.202500168.

[43] F. Zheng, M. Kotobuki, S. Song, M.O. Lai, L. Lu, Review on solid electrolytes for all-solid-state lithium-ion batteries, J. Power Sources 389 (Jun. 2018) 198–213, https://doi.org/10.1016/j.jpowsour.2018.04.022.

[44] X. Lü, et al., Antiperovskite Li $_3$ OCl superionic conductor films for solid-state Li-Ion batteries, Adv. Sci. 3 (3) (Mar. 2016), https://doi.org/10.1002/advs.201500359.

[45] S. Liu, et al., Efficient photocatalytic hydrogen evolution over carbon supported antiperovskite cobalt zinc nitride, Chem. Eng. J. 408 (Mar. 2021) 127307, https://doi.org/10.1016/j.cej.2020.127307.

[46] S. Nishioka, F.E. Osterloh, X. Wang, T.E. Mallouk, K. Maeda, Photocatalytic water splitting, Nat. Rev. Methods Prim. 3 (1) (Jun. 2023) 42, https://doi.org/10.1038/s43586-023-00226-x.

[47] C. Kang, S. Lian, C. Li, J. Ren, M. Chen, Micro-mechanism investigation of hydrogen evolution reaction on anti-perovskite Ni3InN considering doping and strain effects, Appl. Surf. Sci. 652 (Apr. 2024) 159366, https://doi.org/10.1016/j.apsusc.2024.159366.

[48] A.L. Bédé, et al., Theoretical study by density functional theory method (DFT) of stability, tautomerism, reactivity and prediction of acidity of Quinolein-4-one derivatives, Comput. Chem. 06 (03) (2018) 57–70, https://doi.org/10.4236/cc.2018.63005.

[49] J.P. Perdew, A. Zunger, Self-interaction correction to density-functional approximations for many-electron systems, Phys. Rev. B 23 (10) (May 1981) 5048–5079, https://doi.org/10.1103/PhysRevB.23.5048.

[50] P. Giannozzi, et al., QUANTUM ESPRESSO: a modular and open-source software project for quantum simulations of materials, J. Phys. Condens. Matter 21 (39) (Sep. 2009) 395502, https://doi.org/10.1088/0953-8984/21/39/395502.

[51] G. Kresse, J. Hafner, Norm-conserving and ultrasoft pseudopotentials for first-row and transition elements, J. Phys. Condens. Matter 6 (40) (Oct. 1994) 8245–8257, https://doi.org/10.1088/0953-8984/6/40/015.

[52] P. Haas, F. Tran, P. Blaha, K. Schwarz, Construction of an optimal GGA functional for molecules and solids, Phys. Rev. B 83 (20) (May 2011) 205117, https://doi.org/10.1103/PhysRevB.83.205117.

[53] Z. Wu, R.E. Cohen, More accurate generalized gradient approximation for solids, Phys. Rev. B 73 (23) (Jun. 2006) 235116, https://doi.org/10.1103/PhysRevB.73.235116.

[54] P. Giannozzi, et al., Advanced capabilities for materials modelling with Quantum ESPRESSO, J. Phys. Condens. Matter 29 (46) (Nov. 2017) 465901, https://doi.org/10.1088/1361-648X/aa8f79.

[55] H.S. Patel, V.A. Dabhi, A.M. Vora, Adverse effect of K-Mesh shifting in several crystal systems: an analytical study, Mater. Today Proc. 57 (2022) 275–278, https://doi.org/10.1016/j.matpr.2022.02.599.

[56] D.R. Hamann, M. Schlüter, C. Chiang, Norm-conserving pseudopotentials, Phys. Rev. Lett. 43 (20) (Nov. 1979) 1494–1497, https://doi.org/10.1103/PhysRevLett.43.1494.

[57] F. Karsch, A. Patkós, P. Petreczky, Screened perturbation theory, Phys. Lett. B 401 (1–2) (May 1997) 69–73, https://doi.org/10.1016/S0370-2693(97)00392-4.

[58] A.A. Aloufi, Z.A. Alahmed, A. Laref, H.A. Albrithen, Strain effects on structural, electronic, and optical properties of BeO by DFT, Mater. Res Bull. 114 (Jun. 2019) 52–60, https://doi.org/10.1016/j.materresbull.2019.02.015.

[59] S. Kahlaoui, B. Belhorma, H. Labrim, M. Boujnah, M. Regragui, Strain effects on the electronic, optical and electrical properties of Cu2ZnSnS4: DFT study, Heliyon 6 (4) (Apr. 2020) e03713, https://doi.org/10.1016/j.heliyon.2020.e03713.

[60] P.D. Sreedevi, R. Vidya, P. Ravindran, Antiperovskite materials as promising candidates for efficient tandem photovoltaics: first-principles investigation, Mater. Sci. Semicond. Process 147 (Aug. 2022) 106727, https://doi.org/10.1016/j.mssp.2022.106727.

[61] R. Jacobs, J. Booske, D. Morgan, Understanding and controlling the work function of perovskite oxides using density functional theory, Adv. Funct. Mater. 26 (30) (Aug. 2016) 5471–5482, https://doi.org/10.1002/adfm.201600243.

[62] T. Ma, R. Jacobs, J. Booske, D. Morgan, Discovery and engineering of low work function perovskite materials, J. Mater. Chem. C Mater. 9 (37) (2021) 12778–12790, https://doi.org/10.1039/D1TC01286J.

[63] X. Feng, et al., Linear regulation of perovskite work function through organic molecular layer surface modification, Appl. Phys. Lett. 126 (14) (Apr. 2025), https://doi.org/10.1063/5.0253275.

[64] M. Ezzeldien, et al., Electronic and optical properties of bulk and surface of CsPbBr3 inorganic halide perovskite a first principles DFT 1/2 approach, Sci. Rep. 11 (1) (Oct. 2021) 20622, https://doi.org/10.1038/s41598-021-99551-y.

[65] K. Deepthi Jayan, V. Sebastian, Comprehensive device modelling and performance analysis of MASnI3 based perovskite solar cells with diverse ETM, HTM and back metal contacts, Sol. Energy 217 (Mar. 2021) 40–48, https://doi.org/10.1016/j.solener.2021.01.058.

[66] S. Karthick, S. Velumani, J. Bouclé, Chalcogenide BaZrS3 perovskite solar cells: a numerical simulation and analysis using SCAPS-1D, Opt. Mater. 126 (Apr. 2022), https://doi.org/10.1016/j.optmat.2022.112250.

[67] M. Burgelman, K. Decock, S. Khelifi, A. Abass, Advanced electrical simulation of thin film solar cells, Thin Solid Films 535 (May 2013) 296–301, https://doi.org/10.1016/j.tsf.2012.10.032.

[68] Y. Wang, S. J Laihonen, M. Unge, A.A. Mostofi, Improving the precision of work-function calculations within plane-wave density functional theory, Electron. Struct. 6 (3) (Sep. 2024) 037004, https://doi.org/10.1088/2516-1075/ad72c2.

[69] H. Abedini-Ahangarkola, S. SoleimaniAmiri, S. Gholami Rudi, Modeling and numerical simulation of high efficiency perovskite solar cell with three active layers, Sol. Energy 236 (Apr. 2022) 724–732, https://doi.org/10.1016/j.solener.2022.03.055.

[70] Q.-Q. Liang, et al., First-principles calculations to investigate structural, electronic, optical and thermodynamic properties of anti-perovskite compounds X3OI(X = Na, K, Rb), J. Mater. Res. Technol. 22 (Jan. 2023) 3245–3254, https://doi.org/10.1016/j.jmrt.2022.12.148.

[71] Z. Lv, H. Cui, H. Wang, X. Li, G. Ji, Electronic, elastic, lattice dynamic and thermal conductivity properties of Na3OBr via first principles, Phys. Status Solidi (b) 254 (9) (Sep. 2017), https://doi.org/10.1002/pssb.201700089.

[72] S.A. Khandy, I. Islam, A. Laref, M. Gogolin, A.K. Hafiz, A.M. Siddiqui, Electronic structure, thermomechanical and phonon properties of inverse perovskite oxide (Na 3 OCl): an ab initio study, Int J. Energy Res 44 (4) (Mar. 2020) 2594–2603, https://doi.org/10.1002/er.4982.

[73] A.H. Reshak, et al., Exploration of the electronic structure of monoclinic α-Eu 2 (MoO 4) 3: DFT-based study and X-ray photoelectron spectroscopy, J. Phys. Chem. C. 120 (19) (May 2016) 10559–10568, https://doi.org/10.1021/acs.jpcc.6b01489.

[74] Y.N. Zhuravlev, V.V. Atuchin, Comprehensive density functional theory studies of vibrational spectra of carbonates, Nanomaterials 10 (11) (Nov. 2020) 2275, https://doi.org/10.3390/nano10112275.

[75] C. Sun, et al., Tuning electronic properties of epitaxial multilayer-graphene/4H–SiC(0001) by Joule heating decomposition in hydrogen, J. Phys. Chem. Solids 137 (Feb. 2020) 109224, https://doi.org/10.1016/j.jpcs.2019.109224.

[76] A. Togo, I. Tanaka, First principles phonon calculations in materials science, Scr. Mater. 108 (Nov. 2015) 1–5, https://doi.org/10.1016/j.scriptamat.2015.07.021.

[77] M. Hong, et al., Realizing zT of 2.3 in Ge $1-x-y$ Sb x In y Te via reducing the phase-transition temperature and introducing resonant energy doping, Adv. Mater. 30 (11) (Mar. 2018), https://doi.org/10.1002/adma.201705942.

[78] A. Sharma, P. Suryanarayana, Calculation of phonons in real-space density functional theory, Phys. Rev. E 108 (4) (Oct. 2023) 045302, https://doi.org/10.1103/PhysRevE.108.045302.

[79] E. Mohebbi, E. Pavoni, D. Mencarelli, P. Stipa, E. Laudadio, L. Pierantoni, Stability, phonon calculations, electronic structure, and optical properties of a VO2(M) nanostructure: a comprehensive density functional theory study, Front Mater. 10 (Feb. 2023), https://doi.org/10.3389/fmats.2023.1145822.

[80] W. Sun, L. Li, J. Zhang, H. Yin, Theoretical study of phonon dispersion of lanthanum aluminate in terahertz frequency, Procedia Comput. Sci. 147 (2019) 90–96, https://doi.org/10.1016/j.procs.2019.01.196.

[81] K.P.V. Robles, J.-J. Yee, S.-H. Kee, Effect of the geometrical constraints to the Wenner four-point electrical resistivity test of reinforced concrete slabs, Sensors 21 (13) (Jul. 2021) 4622, https://doi.org/10.3390/s21134622.

[82] D. Lu, et al., Down regulation of CIAPIN1 reverses multidrug resistance in human breast cancer cells by inhibiting MDR1, Molecules 17 (6) (Jun. 2012) 7595–7611, https://doi.org/10.3390/molecules17067595.

[83] F. Mouhat, F.-X. Coudert, Necessary and sufficient elastic stability conditions in various crystal systems, Phys. Rev. B 90 (22) (Dec. 2014) 224104, https://doi.org/10.1103/PhysRevB.90.224104.

[84] N. Erum, J. Ahmad, Structural, elastic and mechanical properties of cubic perovskite materials, Arch. Adv. Eng. Sci. 2 (1) (Jun. 2023) 24–29, https://doi.org/10.47852/bonviewAAES3202944.

[85] B. Rehmat, M.A. Rafiq, Y. Javed, Z. Irshad, N. Ahmed, S.M. Mirza, Elastic properties of perovskite-type hydrides LiBeH3 and NaBeH3 for hydrogen storage, Int J. Hydrog. Energy 42 (15) (Apr. 2017) 10038–10046, https://doi.org/10.1016/j.ijhydene.2017.01.109.

[86] M.I. Naher, M.A. Afzal, S.H. Naqib, A comprehensive DFT based insights into the physical properties of tetragonal superconducting Mo5PB2, Results Phys. 28 (Sep. 2021) 104612, https://doi.org/10.1016/j.rinp.2021.104612.

[87] M.E. Eberhart, T.E. Jones, Cauchy pressure and the generalized bonding model for nonmagnetic bcc transition metals, Phys. Rev. B 86 (13) (Oct. 2012) 134106, https://doi.org/10.1103/PhysRevB.86.134106.

[88] M.I. Naher, S.H. Naqib, An ab-initio study on structural, elastic, electronic, bonding, thermal, and optical properties of topological Weyl semimetal TaX (X = P, As), Sci. Rep. 11 (1) (Mar. 2021) 5592, https://doi.org/10.1038/s41598-021-85074-z.

[89] O.N. Senkov, D.B. Miracle, Generalization of intrinsic ductile-to-brittle criteria by Pugh and Pettifor for materials with a cubic crystal structure, Sci. Rep. 11 (1) (Feb. 2021) 4531, https://doi.org/10.1038/s41598-021-83953-z.

[90] S. Daoud, Sound velocities and Debye temperature of BeSe under high pressure up to 50 GPa, Int. J. Phys. Res. 5 (1) (Dec. 2016) 7–10, https://doi.org/10.14419/ijpr.v5i1.7013.

[91] P. Kuchhal, N. Dass, A new model to study the sound velocity in liquid metals, Gazi Univ. J. Sci. (Jul. 2025), https://doi.org/10.35378/gujs.1502124.

[92] S. Speziale, S.R. Shieh, T.S. Duffy, High-pressure elasticity of calcium oxide: a comparison between Brillouin spectroscopy and radial X-ray diffraction, J. Geophys. Res. Solid Earth 111 (B2) (Feb. 2006), https://doi.org/10.1029/2005JB003823.

[93] X. Du, D. He, H. Mei, Y. Zhong, N. Cheng, Insights on electronic structures, elastic features and optical properties of mixed-valence double perovskites Cs2Au2X6 (X=F, Cl, Br, I), Phys. Lett. A 384 (8) (Mar. 2020) 126169, https://doi.org/10.1016/j.physleta.2019.126169.

[94] Y. Liu, X. Zhang, H. Bi, X. Liu, F. Wang, First-principles prediction of structure, mechanical and thermodynamic properties of BixGeyOz ternary bismuth crystals, Vacuum 195 (Jan. 2022) 110696, https://doi.org/10.1016/j.vacuum.2021.110696.

[95] D.-Y. Hu, et al., First-principles calculations to investigate the structural, electronic and optical properties of lead-free double perovskites Rb2SeI6 and K2SeI6, Sol. Energy 231 (Jan. 2022) 236–242, https://doi.org/10.1016/j.solener.2021.11.062.

[96] X. Shi, et al., Highly Efficient ultra-thin solar selective absorber based on Self-assembled tangent Nano-Ball-Cap arrays, Chem. Eng. J. 505 (Feb. 2025) 159459, https://doi.org/10.1016/j.cej.2025.159459.

[97] Md.F. Rahman, et al., The optical and electronic properties of inorganic halide perovskite Sr3NCl3 under applied biaxial strain, J. Mater. Sci. 58 (32) (Aug. 2023) 13100–13117, https://doi.org/10.1007/s10853-023-08825-5.

[98] A. Ghosh, et al., Inorganic novel cubic halide perovskite Sr3AsI3: strain-activated electronic and optical properties, Heliyon 9 (8) (Aug. 2023) e19271, https://doi.org/10.1016/j.heliyon.2023.e19271.

[99] Md.F. Rahman, et al., Unraveling the strain-induced and spin–orbit coupling effect of novel inorganic halide perovskites of Ca3AsI3 using DFT, AIP Adv. 13 (8) (Aug. 2023), https://doi.org/10.1063/5.0156961.

[100] A. Ghosh, et al., Investigating of novel inorganic cubic perovskites of A3BX3 (A=Ca, Sr, B P, As, X=I, Br) and their photovoltaic performance with efficiency over 28, J. Alloy. Compd. 986 (May 2024) 174097, https://doi.org/10.1016/j.jallcom.2024.174097.

[101] J.O. Vasseur, P.A. Deymier, L. Dobrzynski, J. Choi, Electronic band gaps in one-dimensional comb structures of simple metals, J. Phys. Condens. Matter 10 (40) (Oct. 1998) 8973–8981, https://doi.org/10.1088/0953-8984/10/40/005.

[102] L. Huang, Z. Chen, J. Li, Effects of strain on the band gap and effective mass in two-dimensional monolayer GaX (X = S, Se, Te), RSC Adv. 5 (8) (2015) 5788–5794, https://doi.org/10.1039/C4RA12107D.

[103] S. Tariq, L.H. Omari, F. Mezzat, E.K. Hlil, Investigation of structural, electronic, optical, and photocatalytic properties of new double perovskites Cs2InSbX6 (X = F, Cl) under strain effects, Heliyon 10 (22) (Nov. 2024) e40315, https://doi.org/10.1016/j.heliyon.2024.e40315.

[104] J. Wei, Y. Guo, G. Wang, Effects of isotropic strain on the structure and transport properties of half-Heusler alloy BiBaK: a first-principles investigation, RSC Adv. 14 (1) (2024) 463–477, https://doi.org/10.1039/D3RA07345A.

[105] C.-H. Ri, Y.-S. Kim, U.-G. Jong, Y.-H. Kye, S.-H. Ryang, C.-J. Yu, First-principles study on structural, electronic and optical properties of perovskite solid solutions KB 1−x MgxI3 (B = Ge, Sn) toward water splitting photocatalysis, RSC Adv. 11 (42) (2021) 26432–26443, https://doi.org/10.1039/D1RA04534B.

[106] J. Xu, W. Wang, S. Sun, L. Wang, Enhancing visible-light-induced photocatalytic activity by coupling with wide-band-gap semiconductor: a case study on Bi2WO6/TiO2, Appl. Catal. B 111–112 (Jan. 2012) 126–132, https://doi.org/10.1016/j.apcatb.2011.09.025.

[107] S. Saleem, et al., A band gap engineering for the modification in electrical properties of Fe3O4 by Cu2+ doping for electronic and optoelectronic devices applications, J. Solgel Sci. Technol. 109 (2) (Feb. 2024) 471–482, https://doi.org/10.1007/s10971-023-06287-4.

[108] M. Kumar, S. Rani, Y. Singh, K.S. Gour, V.N. Singh, Tin-selenide as a futuristic material: properties and applications, RSC Adv. 11 (12) (2021) 6477–6503, https://doi.org/10.1039/D0RA09807H.

[109] Y. Gu, J.P. Romankiewicz, J.K. David, J.L. Lensch, L.J. Lauhon, Quantitative measurement of the electron and hole mobility−lifetime products in semiconductor nanowires, Nano Lett. 6 (5) (May 2006) 948–952, https://doi.org/10.1021/nl052576y.

[110] S. Mamoun, A.E. Merad, New eco-friendly Rb2PtI6 based double perovskite solar cells with high photovoltaic performance up to 26% efficiency: numerical simulation, Renew. Energy 240 (Feb. 2025) 122268, https://doi.org/10.1016/j.renene.2024.122268.

[111] E.R. Burmistrov, L.P. Avakyants, M.M. Afanasova, Piezoelectric relaxation of two-dimensional electron gas in heterostructures with InGaN/GaN quantum wells,

Russ. Phys. J. 64 (5) (Sep. 2021) 770–782, https://doi.org/10.1007/s11182-021-02391-6.
[112] D.M. Caughey, R.E. Thomas, Carrier mobilities in silicon empirically related to doping and field, Proc. IEEE 55 (12) (1967) 2192–2193, https://doi.org/10.1109/PROC.1967.6123.
[113] W. Liu, X. Yan, G. Chen, Z. Ren, "Recent advances in thermoelectric nanocomposites, Nano Energy 1 (1) (Jan. 2012) 42–56, https://doi.org/10.1016/J.NANOEN.2011.10.001.
[114] Brennan and K. F, The Physics of Semiconductors. 1999. Accessed: Jun. 12, 2025, (Online). Available: ⟨https://ui.adsabs.harvard.edu/abs/1999phse.book……B/abstract⟩.
[115] C. Zhang, R. Wang, H. Mishra, and Y. Liu, "Two-Dimensional Semiconductors with High Intrinsic Carrier Mobility at Room Temperature," 2023, https://doi.org/10.1103/PhysRevLett.130.087001.
[116] S.H. Mir, V.K. Yadav, J.K. Singh, J.K. Singh, Recent advances in the carrier mobility of two-dimensional materials: a theoretical perspective, ACS Omega 5 (24) (Jun. 2020) 14203–14211, https://doi.org/10.1021/ACSOMEGA.0C01676/ASSET/IMAGES/LARGE/AO0C01676_0003.JPEG.
[117] L. Cheng, C. Zhang, Y. Liu, Intrinsic charge carrier mobility of 2D semiconductors, Comput. Mater. Sci. 194 (Jun. 2021) 110468, https://doi.org/10.1016/J.COMMATSCI.2021.110468.
[118] Y. Zhai, et al., Individual electron and hole mobilities in lead-halide perovskites revealed by noncontact methods, ACS Energy Lett. 5 (1) (Jan. 2020) 47–55, https://doi.org/10.1021/acsenergylett.9b02310.
[119] M.T. Ilyas, K. Kaur, J. Sharma, G.S.S. Saini, DFT study of electronic structure and mobility of pristine and fluorinated methylammonium lead halide perovskites (CH3NH3PbX3, X = I, Br, Cl), Int J. Energy Res 46 (5) (Apr. 2022) 6889–6900, https://doi.org/10.1002/er.7623.
[120] J. Lim, et al., Long-range charge carrier mobility in metal halide perovskite thin-films and single crystals via transient photo-conductivity, Nat. Commun. 13 (1) (Jul. 2022) 4201, https://doi.org/10.1038/s41467-022-31569-w.
[121] Z. Zhang, B. Saparov, Charge carrier mobility of halide perovskite single crystals for ionizing radiation detection, Appl. Phys. Lett. 119 (3) (Jul. 2021), https://doi.org/10.1063/5.0057411.
[122] P.K. Nayak, N. Periasamy, Calculation of electron affinity, ionization potential, transport gap, optical band gap and exciton binding energy of organic solids using 'solvation' model and DFT, Org. Electron 10 (7) (Nov. 2009) 1396–1400, https://doi.org/10.1016/j.orgel.2009.06.011.
[123] L. Lin, R. Jacobs, T. Ma, D. Chen, J. Booske, D. Morgan, Work function: fundamentals, measurement, calculation, engineering, and applications, Phys. Rev. Appl. 19 (3) (Mar. 2023) 037001, https://doi.org/10.1103/PhysRevApplied.19.037001.
[124] C. Kaewmeechai, Y. Laosiritaworn, A.P. Jaroenjittichai, Band alignment of Cs2BX6 double halide perovskites and TiO2 using electron affinity rule, Results Phys. 42 (Nov. 2022) 106015, https://doi.org/10.1016/j.rinp.2022.106015.
[125] S. Kashiwaya, J. Morasch, V. Streibel, T. Toupance, W. Jaegermann, A. Klein, The work function of TiO2, Surfaces 1 (1) (Sep. 2018) 73–89, https://doi.org/10.3390/surfaces1010007.
[126] M. Chen, et al., Cesium Titanium(IV) Bromide thin films based stable lead-free perovskite solar cells, Joule 2 (3) (Mar. 2018) 558–570, https://doi.org/10.1016/j.joule.2018.01.009.
[127] H. Kim, H.J. Choi, Thickness dependence of work function, ionization energy, and electron affinity of Mo and W dichalcogenides from DFT and GW calculations, Phys. Rev. B 103 (8) (Feb. 2021) 085404, https://doi.org/10.1103/PhysRevB.103.085404.
[128] H.R. Atapattu, et al., A'-site dipole magnitude and direction dominate the ionization energy and electron affinity of layered metal-halide perovskites, J. Am. Chem. Soc. 147 (30) (Jul. 2025) 26898–26906, https://doi.org/10.1021/jacs.5c08621.
[129] I. Musa, N. Qamhieh, J. Ghabboun, S.T. Mahmoud, Investigation of tunable work function, electrostatic force microscopy and band structure of TiO2 nanoparticles using Kelvin probe force microscopy, Materials 9 (Oct. 2025) 101088, https://doi.org/10.1016/j.nxmate.2025.101088.
[130] M. Wei, C.-F. Li, X.-R. Deng, H. Deng, Surface work function of transparent conductive ZnO films, Energy Procedia 16 (2012) 76–80, https://doi.org/10.1016/j.egypro.2012.01.014.
[131] J. Xu, W. Wang, S. Sun, L. Wang, Enhancing visible-light-induced photocatalytic activity by coupling with wide-band-gap semiconductor: a case study on Bi2WO6/TiO2, Appl. Catal. B 111–112 (Jan. 2012) 126–132, https://doi.org/10.1016/j.apcatb.2011.09.025.
[132] C.-H. Ri, Y.-S. Kim, U.-G. Jong, Y.-H. Kye, S.-H. Ryang, C.-J. Yu, First-principles study on structural, electronic and optical properties of perovskite solid solutions KB 1−x Mg x I 3 (B = Ge, Sn) toward water splitting photocatalysis, RSC Adv. 11 (42) (2021) 26432–26443, https://doi.org/10.1039/D1RA04534B.
[133] T.-N. Do, et al., Electronic and photocatalytic properties of two-dimensional boron phosphide/SiC van der Waals heterostructure with direct type-II band alignment: a first principles study, RSC Adv. 10 (53) (2020) 32027–32033, https://doi.org/10.1039/D0RA05579D.
[134] V. Stevanović, S. Lany, D.S. Ginley, W. Tumas, A. Zunger, Assessing capability of semiconductors to split water using ionization potentials and electron affinities only, Phys. Chem. Chem. Phys. 16 (8) (2014) 3706, https://doi.org/10.1039/c3cp54589j.
[135] S. Nishioka, F.E. Osterloh, X. Wang, T.E. Mallouk, K. Maeda, Photocatalytic water splitting, Nat. Rev. Methods Prim. 3 (1) (Jun. 2023) 42, https://doi.org/10.1038/s43586-023-00226-x.
[136] Y. Rouzhahong, M. Wushuer, M. Mamat, Q. Wang, Q. Wang, First principles calculation for photocatalytic activity of GaAs monolayer, Sci. Rep. 10 (1) (Jun. 2020) 9597, https://doi.org/10.1038/s41598-020-66575-9.
[137] X. Peng, Q. Wei, A. Copple, Strain-engineered direct-indirect band gap transition and its mechanism in two-dimensional phosphorene, Phys. Rev. B 90 (8) (Aug. 2014) 085402, https://doi.org/10.1103/PhysRevB.90.085402.
[138] H. Sabbah, Z. Abdel Baki, R. Mezher, J. Arayro, SCAPS-1D modeling of hydrogenated lead-free Cs2AgBiBr6 double perovskite solar cells with a remarkable efficiency of 26.3, Nanomaterials 14 (1) (Dec. 2023) 48, https://doi.org/10.3390/nano14010048.
[139] M. Bilal, S. Jalali-Asadabadi, R. Ahmad, I. Ahmad, Electronic properties of antiperovskite materials from state-of-the-art density functional theory, J. Chem. 2015 (2015) 1–11, https://doi.org/10.1155/2015/495131.
[140] Z. Jia, et al., Applications of all-inorganic perovskites for energy storage, Mater. Adv. 4 (1) (2023) 79–104, https://doi.org/10.1039/d2ma00779g.
[141] W. Xia, et al., Antiperovskite electrolytes for solid-state batteries, Chem. Rev. 122 (3) (Feb. 2022) 3763–3819, https://doi.org/10.1021/acs.chemrev.1c00594.
[142] Md.A.B. Shanto, et al., Investigating how the electronic and optical properties of a novel cubic inorganic halide perovskite, Sr3NI3 are affected by strain, F1000Res 12 (Aug. 2023) 1005, https://doi.org/10.12688/f1000research.137044.1.
[143] S. Niu, X. Liu, C. Wang, W. Mu, W. Xu, Q. Wang, Breaking the trade-off between complexity and absorbing performance in metamaterials through intelligent design, Small 21 (24) (Jun. 2025), https://doi.org/10.1002/smll.202502828.
[144] Md.S. Islam, et al., Investigation strain effects on the electronic, optical, and output performance of the novel inorganic halide perovskite Sr3SbI3 solar cell, Chin. J. Phys. 88 (Apr. 2024) 270–286, https://doi.org/10.1016/j.cjph.2024.01.011.
[145] Z. Xie, L. Hui, J. Wang, G. Zhu, Z. Chen, C. Li, Electronic and optical properties of monolayer black phosphorus induced by bi-axial strain, Comput. Mater. Sci. 144 (Mar. 2018) 304–314, https://doi.org/10.1016/j.commatsci.2017.12.026.
[146] Y.H. Wong, V.V. Atuchin, V.N. Kruchinin, K.Y. Cheong, Physical and dispersive optical characteristics of ZrON/Si thin-film system, Appl. Phys. A 115 (3) (Jun. 2014) 1069–1072, https://doi.org/10.1007/s00339-013-7947-1.
[147] M. Bhatt, K. Gautam, A. Verma, A.K. Sinha, Structural, optical, surface chemical, and electrochemical characterization of Aloe vera-assisted ZnO nanostructures for supercapattery applications, Mater. Adv. 6 (16) (2025) 5618–5632, https://doi.org/10.1039/D5MA00556F.
[148] A.S. Saidov, et al., Processes of current transport in p-Si-n-$(Si_2)_{1-y-z}(GaP)_y(ZnSe)_z$ heterostructure produced by liquid phase epitaxy, eJ. Surf. Sci. Nanotechnol. 21 (1) (Dec. 2022), https://doi.org/10.1380/ejssnt.2023-009.
[149] A.B. Kuzmenko, Kramers–Kronig constrained variational analysis of optical spectra, Rev. Sci. Instrum. 76 (8) (Aug. 2005), https://doi.org/10.1063/1.1979470.
[150] S. Chen, G. Xu, X. Zhang, T. Peng, Y. Sun, X. Wang, Strain-dependent work function of metal surfaces: insights from first-principles investigation, Phys. B Condens Matter 690 (Oct. 2024) 416288, https://doi.org/10.1016/j.physb.2024.416288.
[151] Md.E. Ali, DFT-based investigation of optoelectronic, dynamic, thermodynamic, mechanical, and strain-engineered properties of a novel lead-free Na3SBr inorganic anti-perovskite and achieving over 27% solar cell efficiency, J. Alloy. Compd. 1043 (Oct. 2025) 184221, https://doi.org/10.1016/j.jallcom.2025.184221.
[152] X. Nie, Z. Yu, E. Jackson, J. Lee, Refractive index and extinction coefficient of hollow microspheres for solar reflection, Appl. Phys. Lett. 118 (21) (May 2021), https://doi.org/10.1063/5.0049018.
[153] X. Ziang, et al., Refractive index and extinction coefficient of CH_3NH_3PbI_3 studied by spectroscopic ellipsometry, Opt. Mater. Express 5 (1) (Jan. 2015) 29, https://doi.org/10.1364/OME.5.000029.
[154] C. Claeys, E. Simoen. Radiation Effects in Advanced Semiconductor Materials and Devices, Springer Berlin Heidelberg, Berlin, Heidelberg, 2002, 5710.1007/978-3-662-04974-7.
[155] J. Grum, Book review: electronic and optoelectronic properties of semiconductor structures by Jasprit Singh, Int. J. Microstruct. Mater. Prop. 4 (3) (2009) 391, https://doi.org/10.1504/IJMMP.2009.031146.
[156] Bhattacharya, Pallab, Semiconductor optoelectronic devices, Choice Rev. Online 31 (08) (Apr. 1994) 31-4379–31–4379, https://doi.org/10.5860/CHOICE.31-4379.
[157] B.E.A. Saleh, M.C. Teich, Fundamentals of Photonics, Wiley, 1991, https://doi.org/10.1002/0471213748.
[158] X. Fu, Z. Niu, C. Peng, H. Han, W. Sun, T. Yue, Quantitative synergistic adsorption affinity of Ca(II) and sodium oleate to predict the surface reactivity of hematite and quartz, Sep Purif. Technol. 360 (Jul. 2025) 131196, https://doi.org/10.1016/j.seppur.2024.131196.
[159] J. Yu, et al., Regulating socketed geometry of nanoparticles on perovskite oxide supports for enhanced stability in oxidation reactions, Nat. Commun. 15 (1) (Nov. 2024) 10229, https://doi.org/10.1038/s41467-024-54546-x.
[160] D. Metzner, M. Olbrich, P. Lickschat, A. Horn, S. Weißmantel, Experimental and theoretical determination of the effective penetration depth of ultrafast laser radiation in stainless steel, Lasers Manuf. Mater. Process. 7 (4) (Dec. 2020) 478–495, https://doi.org/10.1007/s40516-020-00129-9.
[161] H.J. Lee, M.M.A. Gamel, P.J. Ker, M.Z. Jamaludin, Y.H. Wong, J.P.R. David, Absorption coefficient of bulk III-V semiconductor materials: a review on methods, properties and future prospects, J. Electron Mater. 51 (11) (Nov. 2022) 6082–6107, https://doi.org/10.1007/s11664-022-09846-7.

[162] A. Nayfeh, S. Abdul Hadi, Si1–Ge deposition and properties. Silicon-Germanium Alloys for Photovoltaic Applications, Elsevier, 2023, pp. 37–61, https://doi.org/10.1016/B978-0-323-85630-0.00003-0.
[163] R.K. Pingak, et al., A DFT investigation of lead-free $TlSnX_3$ (X = Cl, Br, or I) perovskites for potential applications in solar cells and thermoelectric devices, RSC Adv. 13 (48) (2023) 33875–33886, https://doi.org/10.1039/D3RA06685A.
[164] C.R. Cox, J.Z. Lee, D.G. Nocera, T. Buonassisi, Ten-percent solar-to-fuel conversion with nonprecious materials, Proc. Natl. Acad. Sci. 111 (39) (Sep. 2014) 14057–14061, https://doi.org/10.1073/pnas.1414290111.
[165] M.E. Ali, M.M. Haque, S.H. Cheragee, Device modeling and numerical analysis of lead-free MASnI3/Ca3AsI3 based perovskite solar cells with over 38% efficiency, Sol. Energy 288 (2025), https://doi.org/10.1016/j.solener.2025.113309.
[166] I.E. Tinedert, A. Saadoune, M.K. Hossain, A theoretical study of all-inorganic perovskite solar cells: computational modeling of the CsPb3/RbGeI3 bilayer absorber structure, J. Phys. Chem. Solid 189 (2024) 111951, https://doi.org/10.1016/j.jpcs.2024.111951.
[167] N.K. Singh, A. Agarwal, A.K. Singh, S.N. Singh, Design and performance evaluation of eco-friendly FASnI3/CsSn0.5Ge0.5I3 based perovskite solar cell with distinct charge transport layer: a computational modeling, Sol. Energy 268 (2024), https://doi.org/10.1016/j.solener.2023.112256.
[168] X. Shi, et al., Unassisted photoelectrochemical water splitting exceeding 7% solar-to-hydrogen conversion efficiency using photon recycling, Nat. Commun. 7 (1) (Jun. 2016) 11943, https://doi.org/10.1038/ncomms11943.
[169] R.H. Coridan, et al., Methods for comparing the performance of energy-conversion systems for use in solar fuels and solar electricity generation, Energy Environ. Sci. 8 (10) (2015) 2886–2901, https://doi.org/10.1039/C5EE00777A.
[170] J.W. Yang, et al., High-efficiency unbiased water splitting with photoanodes harnessing polycarbazole hole transport layers, Energy Environ. Sci. 17 (7) (2024) 2541–2553, https://doi.org/10.1039/D3EE03353H.
[171] S. Hu, C. Xiang, S. Haussener, A.D. Berger, N.S. Lewis, An analysis of the optimal band gaps of light absorbers in integrated tandem photoelectrochemical water-splitting systems, Energy Environ. Sci. 6 (10) (2013) 2984, https://doi.org/10.1039/c3ee40453f.
[172] M.Y. Chern, D.A. Vennos, F.J. Disalvo, Synthesis, structure, and properties of anti-perovskite nitrides Ca3MN, M=P, As, Sb, Bi, Ge, Sn, and Pb, J. Solid State Chem. 96 (2) (Feb. 1992) 415–425, https://doi.org/10.1016/S0022-4596(05)80276-2.
[173] E. Ahiavi, et al., Mechanochemical synthesis and ion transport properties of Na3OX (X = Cl, Br, I and BH4) antiperovskite solid electrolytes, J. Power Sources 471 (Sep. 2020) 228489, https://doi.org/10.1016/j.jpowsour.2020.228489.
[174] P. Hoffmann, D.I. Villalva-Mejorada, O.W. Elkhafif, T. Diemant, T. Jacob, H. K. Hassan, Is Mg 3 AsN antiperovskite a promising Mg-ion conductor? Mater. Horiz. (2025) https://doi.org/10.1039/D5MH01361E.
[175] H. Fu, et al., Photocatalytic Overall Water Splitting with a Solar-to-Hydrogen Conversion Efficiency Exceeding 2% through Halide Perovskite, Angew. Chem. Int. Ed. 63 (49) (Dec. 2024), https://doi.org/10.1002/anie.202411016.
[176] J.H. Kim, et al., Single junction CsPbBr3 solar cell coupled with electrolyzer for solar water splitting, Nat. Commun. 16 (1) (Jul. 2025) 7003, https://doi.org/10.1038/s41467-025-58980-3.
[177] A. Husainat, W. Ali, P. Cofie, J. Attia, J. Fuller, Simulation and analysis of methylammonium lead iodide (CH3NH3PbI3) perovskite solar cell with Au contact using SCAPS 1D simulator, Am. J. Opt. Photon. 7 (2) (2019) 33, https://doi.org/10.11648/j.ajop.20190702.12.
[178] M. Faghihnasiri, M. Izadifard, M.E. Ghazi, DFT study of mechanical properties and stability of cubic methylammonium lead halide perovskites (CH3NH3PbX3, X = I, Br, Cl), J. Phys. Chem. C 121 (48) (Dec. 2017) 27059–27070, https://doi.org/10.1021/acs.jpcc.7b07129.
[179] A.M.A. Leguy, et al., Dynamic disorder, phonon lifetimes, and the assignment of modes to the vibrational spectra of methylammonium lead halide perovskites, Phys. Chem. Chem. Phys. 18 (39) (2016) 27051–27066, https://doi.org/10.1039/C6CP03474H.
[180] A. ul Rehman, et al., Performance optimization of FASnI3 based perovskite solar cell through SCAPS-1D simulation, Hybrid. Adv. 7 (Dec. 2024) 100301, https://doi.org/10.1016/j.hybadv.2024.100301.
[181] S. Pachori, R. Agrawal, A. Shukla, A. Singh Verma, First-principles calculations for fundamental and spectroscopic screening of hybrid perovskite (HC(NH2) 2PbI3) formamidinium lead iodide, Mater. Chem. Phys. 287 (Aug. 2022) 126149, https://doi.org/10.1016/j.matchemphys.2022.126149.
[182] L. Guo, G. Tang, J. Hong, Mechanical properties of formamidinium halide perovskites FABX 3 (FA= CH(NH2)2; B=Pb, Sn; X=Br, I) by first-principles calculations *, Chin. Phys. Lett. 36 (5) (May 2019) 056201, https://doi.org/10.1088/0256-307X/36/5/056201.
[183] Md.A. Uddin, S. Rahman, T. Zaman, Design and simulation of Cs2SnI6 based perovskite solar cell, Materials 9 (Oct. 2025) 100980, https://doi.org/10.1016/j.nxmate.2025.100980.
[184] U.-G. Jong, C.-J. Yu, Y.-H. Kye, S.-H. Choe, J.-S. Kim, Y.-G. Choe, Anharmonic phonons and phase transitions in the vacancy-ordered double perovskite Cs2SnI6 from first-principles predictions, Phys. Rev. B 99 (18) (May 2019) 184105, https://doi.org/10.1103/PhysRevB.99.184105.
[185] H.-M. Huang, Z.-Y. Jiang, S.-J. Luo, First-principles investigations on the mechanical, thermal, electronic, and optical properties of the defect perovskites Cs2Sn*X*6 (*X* = Cl, Br, I), Chin. Phys. B 26 (9) (Aug. 2017) 096301, https://doi.org/10.1088/1674-1056/26/9/096301.
[186] M.I. Amanyi, et al., SCAPS-1D analysis of non-toxic lead-free MASnI3 perovskite-based solar cell using inorganic charge transport layers, East Eur. J. Phys. (3) (Sep. 2024) 447–455, https://doi.org/10.26565/2312-4334-2024-3-54.
[187] I.O.A. Ali, D.P. Joubert, M.S.H. Suleiman, First-principles study of structural, mechanical, dynamical stability, electronic and optical properties of orthorhombic CH3NH3SnI3 under pressure, Eur. Phys. J. B 92 (9) (Sep. 2019) 202, https://doi.org/10.1140/epjb/e2019-100101-1.
[188] Q.-Q. Liang, et al., First-principles calculations to investigate structural, electronic, optical and thermodynamic properties of anti-perovskite compounds X3OI(X = Na, K, Rb), J. Mater. Res. Technol. 22 (Jan. 2023) 3245–3254, https://doi.org/10.1016/j.jmrt.2022.12.148.